Journal of Materials Research and Technology 41 (2026) 5904–5920

Contents lists available at ScienceDirect

Journal of Materials Research and Technology

journal homepage: www.elsevier.com/locate/jmrt

# Microstructural evolution and its impact on mechanical and corrosion performance of 316L ODS steels processed by mechanical alloying and pulse plasma sintering

Anna Dobkowska [a,*], Kalyan Das [a], Mirosław Jakub Kruszewski [a], Aleksandra Zielińska [a], Marlene González [a], Bogusława Adamczyk-Cieślak [a], Jiří Kubásek [c], Jan Pokorný [c], David Nečas [c], Črtomir Donik [b], Irena Paulin [b], Kamil Majchrowicz [a], Jarosław Mizera [a], Matjaž Godec [b]

[a] Faculty of Materials Science and Engineering, Warsaw University of Technology, Warsaw, Poland
[b] Institute of Metals and Technology, Ljubljana, Slovenia
[c] University of Chemistry and Technology, Prague, Czech Republic

ARTICLE INFO

*Keywords:*
ODS steels
Austenitic steels
Corrosion
Mechanical properties

ABSTRACT

In this study, austenitic oxide dispersion-strengthened (ODS) steels were fabricated by mechanical alloying (MA) of 316L stainless steel with 1 wt% of either nano- or micro-sized $Y_2O_3$ particles, followed by pulse plasma sintering (PPS). The effects of MA duration (5, 10, and 50 h) and $Y_2O_3$ particle size on the microstructure, mechanical properties, and corrosion resistance were systematically investigated. The morphology and size of the alloyed powder particles were strongly influenced by MA parameters: longer milling times produced finer, though more irregularly shaped, particles. Increasing the milling duration led to a higher fraction of fine grains and elevated dislocation densities, indicating grain refinement driven by discontinuous recrystallization. Mechanical testing revealed that strength was primarily controlled by the MA duration. Samples milled for 50 h reached the highest strength regardless of $Y_2O_3$ particle size, owing to the combined effects of grain refinement and Orowan strengthening. This strength gain, however, was accompanied by a loss in ductility. Corrosion behavior, assessed via electrochemical methods and salt spray tests, was strongly dependent on internal strain and grain boundary characteristics. The best corrosion resistance was observed in samples milled for 5 h, which had lower dislocation densities and smaller grain boundary areas. In contrast, prolonged milling (50 h) increased grain boundary density and misorientations, accelerating corrosion—particularly in steels reinforced with micro-sized $Y_2O_3$ particles.

## 1. Introduction

The growing global demand for reliable, sustainable, and affordable energy, without compromising environmental protection, remains a key driver for research and development of advanced nuclear power systems [1]. The primary goal in designing structural materials for nuclear applications is to develop alloys capable of withstanding harsh service conditions, including high temperatures, sustained mechanical loads, chemically aggressive environments, and intense radiation fluxes [2,3]. Oxide dispersion-strengthened (ODS) steels are among the most promising candidates for nuclear fission and fusion reactors, owing to their exceptional high-temperature creep strength and superior radiation resistance [4]. An effective approach to achieving the desired properties is to disperse yttrium oxide ($Y_2O_3$) particles within the steel matrix, as their presence inhibits grain coarsening and suppresses grain boundary sliding [5–7]. This, in turn, improves tensile, yield, and creep strength, as well as corrosion resistance, over a temperature range from room temperature up to approximately 650 °C in ferritic and ferritic–martensitic steels [8–11]. As demonstrated for Fe–18%Cr–2% W-0.2%Ti steels, increasing the $Y_2O_3$ content leads to a higher ultimate tensile strength (UTS), reaching 1394 MPa for 1.5 wt% $Y_2O_3$ [12]. However, the increase in UTS was accompanied by a reduction in elongation. Further improvement of the mechanical properties may be obtained by adding Ti in combination with $Y_2O_3$. As proved by Sing et al.

* Corresponding author.
*E-mail address:* anna.dobkowska@pw.edu.pl (A. Dobkowska).

https://doi.org/10.1016/j.jmrt.2026.02.032
Received 8 October 2025; Received in revised form 1 February 2026; Accepted 3 February 2026
Available online 13 February 2026

[13] during mechanical alloying of 18Cr–2W-0.285Ti-0.5$Y_2O_3$ and Fe–18Cr–2W-0.571Ti–1$Y_2O_3$ wt.%, the $Y_2O_3$ dissociates into Y and O. During consolidation, this leads to the precipitation of various particles: $Y_2O_3$, $TiO_2$, $Cr_2O_3$ with the size around 100 nm and fine $Y_2TiO_5$ and $Y_2Ti_2O_7$ with the size lower than 10 nm. Orthorhombic $Y_2TiO_5$ are incoherent with the ferrite matrix and remain stable up to 1330 °C, whereas $Y_2Ti_2O_7$ are semi-coherent with the matrix. Study of Ordás et al. [14] reported that the presence of $Y_2TiO_5$ and $Y_4Al_2O_9$ effectively controls grain growth, thereby contributing to the stability of mechanical properties. The mechanical behavior of ferritic ODS steels was further investigated by Zhao et al. [15]. The 15Cr–15Ni–Y alloy exhibited a UTS of 887 MPa and a total elongation of 23.5%, whereas the addition of $Y_2O_3$ increased the UTS to 947 MPa, accompanied by a slight reduction in elongation to 21.9%. At 700 °C, the UTS of 15Cr–15Ni–Y dropped to 449 MPa with an elongation of about 15%. Replacing Y with $Y_2O_3$ further improved the UTS to 554 MPa, though elongation was reduced by nearly half. In addition, the fracture behavior changed: at room temperature, a ductile fracture mode was observed, while tests at elevated temperature revealed a mixed ductile–brittle fracture mode.

The design of ODS steels for nuclear applications requires balancing two critical properties: high-temperature mechanical stability and excellent corrosion resistance. However, data on the influence of nano-oxides on the corrosion behavior of $Y_2O_3$ – strengthened ODS steels remain scarce. Although studies on ferritic ODS steels have shown that corrosion resistance is largely independent of $Y_2O_3$ content and is instead governed by alloying elements such as Al [16], Cr [10], V [10] and Ti, the microstructure-dependent corrosion behavior of austenitic ODS steels is still poorly understood. The limited available research indicates that, in ferritic ODS steels, the presence of Cr and Al reduces the corrosion rate by promoting the formation of a stable passive film [17–19].

Nanosized oxide particles in ODS steels are most commonly introduced through mechanical alloying (MA), and the processing parameters have a significant impact on the resulting material properties. Haijian et al. [20] demonstrated that increasing the milling time of ODS ferritic powders with the nominal composition Fe–15Cr–2W-0.3-Ti-0.3Zr-0.3$Y_2O_3$ wt.% led to a progressive reduction in both particle and crystallite sizes, which tended to stabilize after approximately 50 h of milling. The authors further reported that MA promotes the formation of a substructure characterized by fine cells and relatively high misorientation angles. To produce Fe–14Cr–2W-0.5Ti-0.06-Si-0.2V-0.1Mn-0.05Ta-0.03C-0.3$Y_2O_3$, Sun et al. [21] used the sol-gel method followed by 20 h of MA and hot isostatic pressing. Hot isostatic pressing or hot extrusion are commonly used to compress the mechanically alloyed powders [22]. More recently. plasma-assisted techniques such as spark plasma sintering (SPS) and field-assisted sintering (FAST) have been applied, offering lower processing temperatures and shorter sintering times compared to conventional methods [23,24]. Among these, pulse plasma sintering (PPS) provides additional advantages, including even shorter processing times and lower sintering temperatures [25].

In this work, the MAed powders were consolidated by PPS, which belongs to the family of current-assisted powder metallurgy techniques that includes SPS and FAST. In all of these methods, a pulsed electric current is passed through the graphite die and, for electrically conductive systems, through the compact itself, so that Joule heating under uniaxial pressure enables very rapid densification at temperatures and times significantly lower than in conventional hot pressing. PPS employs short, high-intensity electric discharges generated by a capacitor bank; these microsecond pulses locally heat and activate particle surfaces more intensively than in standard SPS/FAST cycles, promoting surface cleaning and accelerated diffusion while still keeping the macroscopic dwell time and peak temperature low. Under the present processing conditions, a dwell of 10 min at 1100 °C and 60 MPa was sufficient to achieve near-theoretical densities in both the reference and ODS steels. A schematic comparison of PPS with SPS/FAST is provided in Supplementary Fig. S1 and Table S1 (adapted from Ref. [26]).

It is important to note that the application of ferritic steels is generally limited to about 650 °C. At higher temperatures, grain coarsening leads to a deterioration of their mechanical properties [27,28], particularly tensile properties and creep resistance [29,30]. In contrast, austenitic ODS steels can operate at higher service temperatures while maintaining mechanical strength, owing to the high thermal stability of oxide particles and their ability to act as effective barriers to dislocation motion [31]. However, the ductile nature of austenitic steels poses challenges during processing, including adhesion of powders to the walls of the milling container during mechanical alloying [32]. This effect can significantly alter the chemical composition of the final powder mixture and, consequently, the microstructure of the consolidated austenitic ODS steels [33].

Given that the properties of ferritic ODS steels are relatively well established, the present study focuses on characterizing the microstructure of ODS 316L stainless steel with $Y_2O_3$ addition fabricated by MA under varying processing parameters and consolidated using PPS. It is well known that the scale of the $Y_2O_3$ feedstock strongly influences its solubility, diffusion and nucleation behavior during processing, the use of nano-crystallized vs micro-crystallized yttria may lead to markedly different densities, distributions, and sizes of the eventual $Y_2O_3$ precipitates [34]. Testing both regimes thus allows us to analyze the precipitate microstructure, and thereby check whether its size is really crucial in mechanical and corrosion properties improvement.

## 2. Materials and methods

### 2.1. Powders preparation

Mixtures of commercially available 316L stainless steel powder (Wolften, Poland, chemical composition given in Table 1) and 1 wt % of $Y_2O_3$ powder (Skyspring Nanomaterials Inc., USA) of two particle size ranges: 1-2 μm (hereafter referred to as micro), and 30-50 nm (hereafter referred to as nano) were subjected to MA. MA was carried out in a planetary ball mill (Retsch® PM100, Germany) for 5, 10, or 50 h without the use of a process control agent. Milling was performed at 250 rpm with a ball-to-powder weight ratio of 5:1, using 15 min milling and 15 min rest intervals, with direction changes between cycles, under an Ar atmosphere. The particle size distribution (PSD) of the powders was measured using a laser scattering particle size analyzer (Horiba LA 950, Japan) in isopropanol suspension, and characterized by D10, D50, D90, and $D_{avg}$ particle size. Powder morphology was examined using scanning electron microscopy (SEM, Axia ChemiSEM, Thermo Scientific, USA). For microstructural observation, powders were mounted in resin and polished with diamond suspensions prior to SEM analysis.

### 2.2. ODS steels fabrication

Consolidation of ODS steels was carried out using the PPS [26] which belongs to the family of current-assisted powder metallurgy techniques, such as SPS and FAST [35]. The PPS approach employs high-current electric pulses that generate heat both in the graphite die and within the powder compact. or this study, the ODS steel powders were loaded into a graphite die with an inner diameter of 25 mm and sintered at a maximum temperature of 1100 °C, using a heating rate of 100 °C/min. The peak temperature was maintained for 10 min under a constant uniaxial pressure of 60 MPa. All processing was conducted under high vacuum ($5 \times 10^{-3}$ Pa) to minimize contamination and oxidation. A reference sample was produced under identical conditions using the as-received 316L powder without prior mechanical alloying.

### 2.3. Microstructure characterization

Microstructural observations were performed using a field-emission scanning electron microscope (FE-SEM JEOL JSM 6500F, Japan). Prior

**Table 1**
Chemical composition of 316L powder according to manufacturer.

| Element (% wt.) | Cr | Ni | Mo | Mn | C | S | Cu | Si | P | Fe |
|---|---|---|---|---|---|---|---|---|---|---|
| Min | 17.50 | 10 | 2.25 | 1.25 | - | | | | | |
| Max | 18.00 | 14 | 2.50 | 2.00 | <0.03 | <0.03 | <0.075 | <0.075 | <0.025 | Bal. |

to imaging, the samples were ion-milled in an Ar + beam. Electron-backscatter diffraction (EBSD) was carried out with a HKL Nordlys II EBSD camera and EDAX software, and the results are presented in the form of inverse pole figures (IPF) and grains average misorientation (GAM) maps. Phase analysis identification was conducted using X-ray diffraction (XRD, Bruker D8 Advance, Germany) operated at 40 kV and 40 mA with Cu–Kα radiation. Diffraction data were collected over a 2θ range of 20–110° with a step size of 0.02° and a count time of 10 s per step. Carbon content in selected samples was measured by combustion analysis using a LECO CHN 628 elemental analyzer (LECO, USA).

Detailed microstructural observations of the ODS steels were carried out using a transmission electron microscope (TEM, JEOL JEM 1200 EX) working at 120 kV. Thin foils for TEM were first mechanically ground and polished to a thickness of approximately 100 μm, then punched into 3 mm diameter discs. The discs were subsequently electropolished using a TENUPOL V system (Struers, Country) with commercial electrolyte A2 (8% perchloric acid, 73% ethanol, 10% 2-butoxyethanol, 9% distilled water) at ~4 °C, under an applied potential of 40 V and 225 mA. Polishing to perforation typically required 1–1.5 min. After polishing, the foils were rinsed twice with ethanol and air-dried. Chemical composition analyses of the powder particles were conducted using a TEM equipped with an energy-dispersive X-ray spectrometer (EDS, Talos, Thermo Fisher Scientific, USA).

### 2.4. Mechanical tests

The mechanical performance of the austenitic ODS steels was tested using a Zwick/Roell Z005 (Germany) testing machine equipped with specialized grips for non-standard micro-sized specimens, as shown by Molak et al. [36]. Miniaturized flat specimens with a cross section of about 0.6 mm × 0.8 mm and a gauge length of 4 mm were used, as described in Majchrowicz et al. [37]. Tensile tests were performed at room temperature at an initial strain rate of 0.001 $s^{-1}$, and strain was measured using a digital image correlation (DIC) system as detailed by Sitek et al. [38]. Characteristic mechanical parameters were determined for each material, including yield strength (YS), ultimate tensile strength (UTS), and percentage elongation after fracture (A) [39]. Five tests were performed for each material to ensure measurement repeatability. Fracture surfaces of the specimens were analyzed using SEM (Axia ChemiSEM, Thermo Scientific, USA). The hardness of the ODS steels was measured using the Brinell method in accordance with ISO 6506 [40]. Measurements were carried out using a Zwick/Roell ZHU2.5 (Germany) hardness testing machine. The samples were polished with silicon carbide (SiC) paper up to #4000 grit. At least five indentations were made on each sample at room temperature, using a cobalt carbide ball indenter with a diameter of 2.5 mm. A load of 2.5 kN was applied for 30 s during each measurement.

### 2.5. Corrosion tests

#### 2.5.1. Corrosion rate

The corrosion rate was calculated based on the weight loss measurements of the samples exposed to salt spray conditions. Salt spray test was performed using concentrated sodium chloride solution (5% NaCl by weight, Chempur, 58.44 g/mol) for 1000 h at a temperature of 35 ± 2 °C according to the standard [41]. The experiment was conducted in CCT 400-FL VDA-I VLM salt chamber. Three independent samples in the form of discs with diameter of 7 mm and approx. 5 mm in height from each material were ground up to P4000, cleaned with ethanol and isopropanol, dried in the air, measured and weighted. After exposition corrosion products were chemically removed by immersion of samples in a mixture of nitric acid ($HNO_3$), hydrofluoric acid (HF) and water in the presence of ultrasounds according to Ref. [42]. The composition of the etchant was composed of consisted of 6.25 mL of $HNO_3$, (Sigma Aldrich, sp gr 1.42), 1.25 mL of HF (Sigma Aldrich, sp gr 1.198-48%) and distilled water to fill up to 62.5 mL. Samples were immersed for 20 min at a temperature of 25 °C in the ultrasonic bath. Afterwards, samples were rinsed with isopropanol for 5 min. Samples were dried naturally and weighed. Corrosion rate was calculated according to the following equation [41]:

$$Corrosion\ rate = \frac{K \cdot W}{A \cdot T \cdot D} \quad (1)$$

where: K = constant 8.76 x $10^7$ (to obtain μm/y as corrosion rate value), T = time in hours, A = area in $cm^2$, W = mass loss in grams and D = density in $g/cm^3$.

The macro images of the corroded samples were made using an optical microscope (VHX-7000, Keyence, Japan). A scanning electron microscope (SU70, Hitachi, Japan) was used to analyze corrosion damage after removal of corrosion products. Cross-sectional observations were made using a combination of a focus ion beam system and scanning electron microscope (FIB/SEM, NB-5000 dual-beam, Hitachi, Japan). The surface roughness was measured using Sensofar metrology S Lynx® optical profilometer (software SensoSCAN6) in confocal mode using an EPI 20x lens (Nikon, Japan) in a 300 × 300 μm area.

## 3. Results

### 3.1. Powder characterization

The morphology and particle size distribution (PSD) of the powders prepared for compaction are presented in Fig. 1. The reference 316L powder exhibits a spherical morphology with an average particle size ($D_{avg}$) of 30 μm. Both particle size and shape evolved with increasing MA duration. For powders modified with either nano- or micro-sized $Y_2O_3$, longer MA times resulted in the formation of larger, more flattened particles. In the case of nano-sized $Y_2O_3$, $D_{avg}$ increased from 83 μm to 277 μm, whereas for micro-sized $Y_2O_3$, it ranged from 50 μm to 280 μm. Quantitatively, D50 increased from 30 μm for the as-received 316L powder to 63 μm (D90 = 172 μm) for the 1 wt% nano-$Y_2O_3$ blend after 5 h of MA, whereas the corresponding micro-doped powder reached only 44 μm (D90 = 77 μm). After 10 h, the D50 values of the nano- and micro-doped powders converged to 60 and 71 μm, respectively, while the upper tail of the distribution remained slightly more pronounced for the nano-doped powder (D90 = 103 vs 96 μm). After 50 h, both series exhibited very coarse agglomerates with comparable D90 values (381 vs 385 μm), and median size (266 vs 267 μm). These trends, together with the broader PSD of the nano-doped powders, support the interpretation that nano-sized $Y_2O_3$ promotes the formation of large flake-like agglomerates through repeated cold welding, whereas the coarser micro-sized oxide more effectively enhances fragmentation and thus moderates agglomerate growth (Fig. S2 and Fig.S3).

The cross-sectional observations of the powder particles prepared by MA for 316L with 1 wt% nano- and micro-sized $Y_2O_3$ additions are shown in Fig. 2. In both cases, milling duration strongly influences particle shape and morphology, with longer MA times producing coarser particles. This effect is particularly pronounced for the nano-sized $Y_2O_3$ (Fig. 2a–c). As shown in Fig. 2d, the particles are enriched in Y, which is

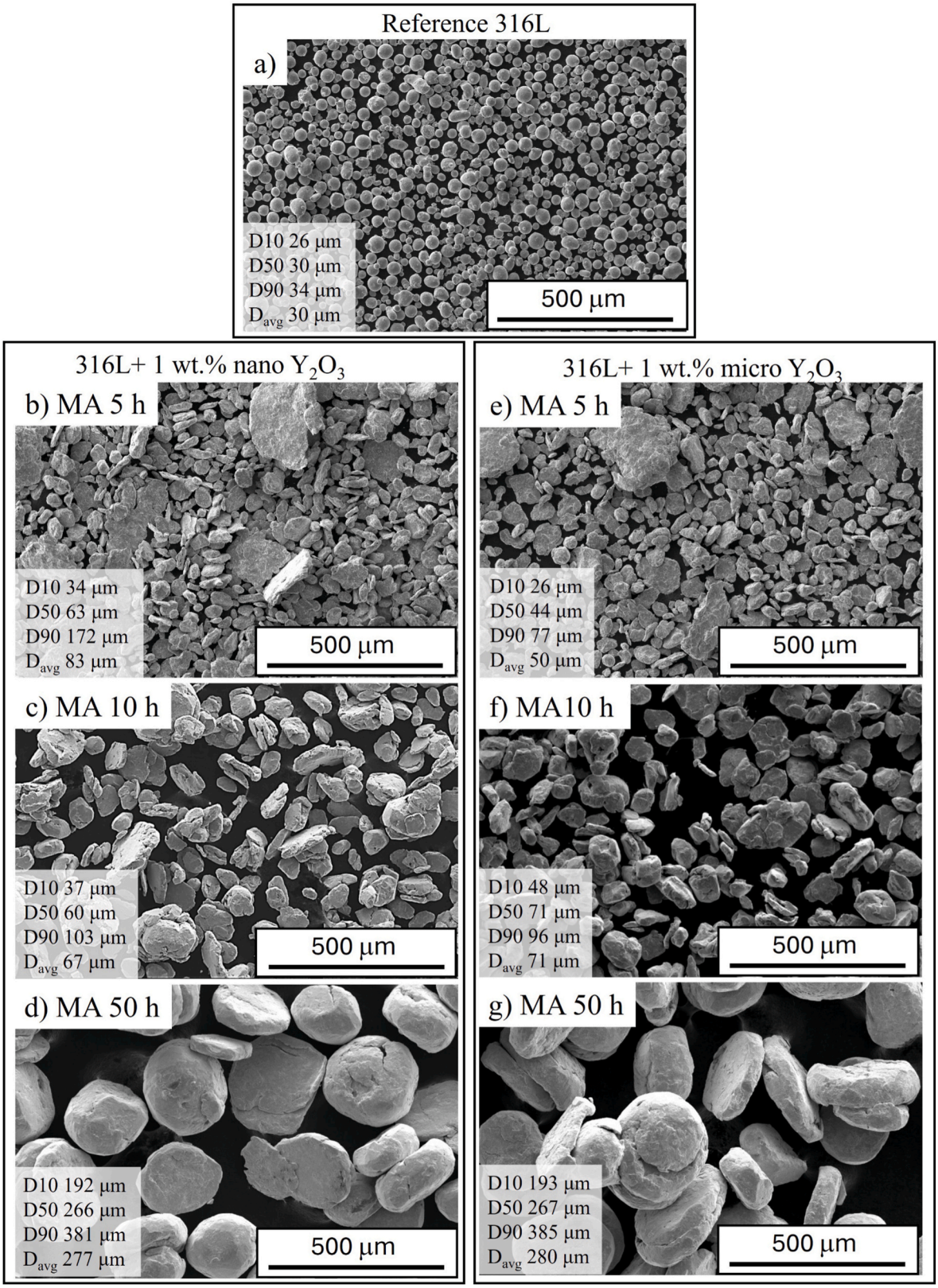


**Fig. 1.** SEM powder morphologies: a) reference 316L powder, 316L with 1 wt% of nano-sized $Y_2O_3$ mechanically alloyed for b) 5 h, c) 10 h, and d) 50 h and, 316L with 1 wt% of micro-sized $Y_2O_3$ mechanically alloyed for e) 5 h, f) 10 h, and g) 50 h. D10, D50 and D90 represent the particle diameters below which 10%, 50% and 90% of total number of particles are found, respectively; $D_{avg}$ denotes the arithmetic mean particle size.

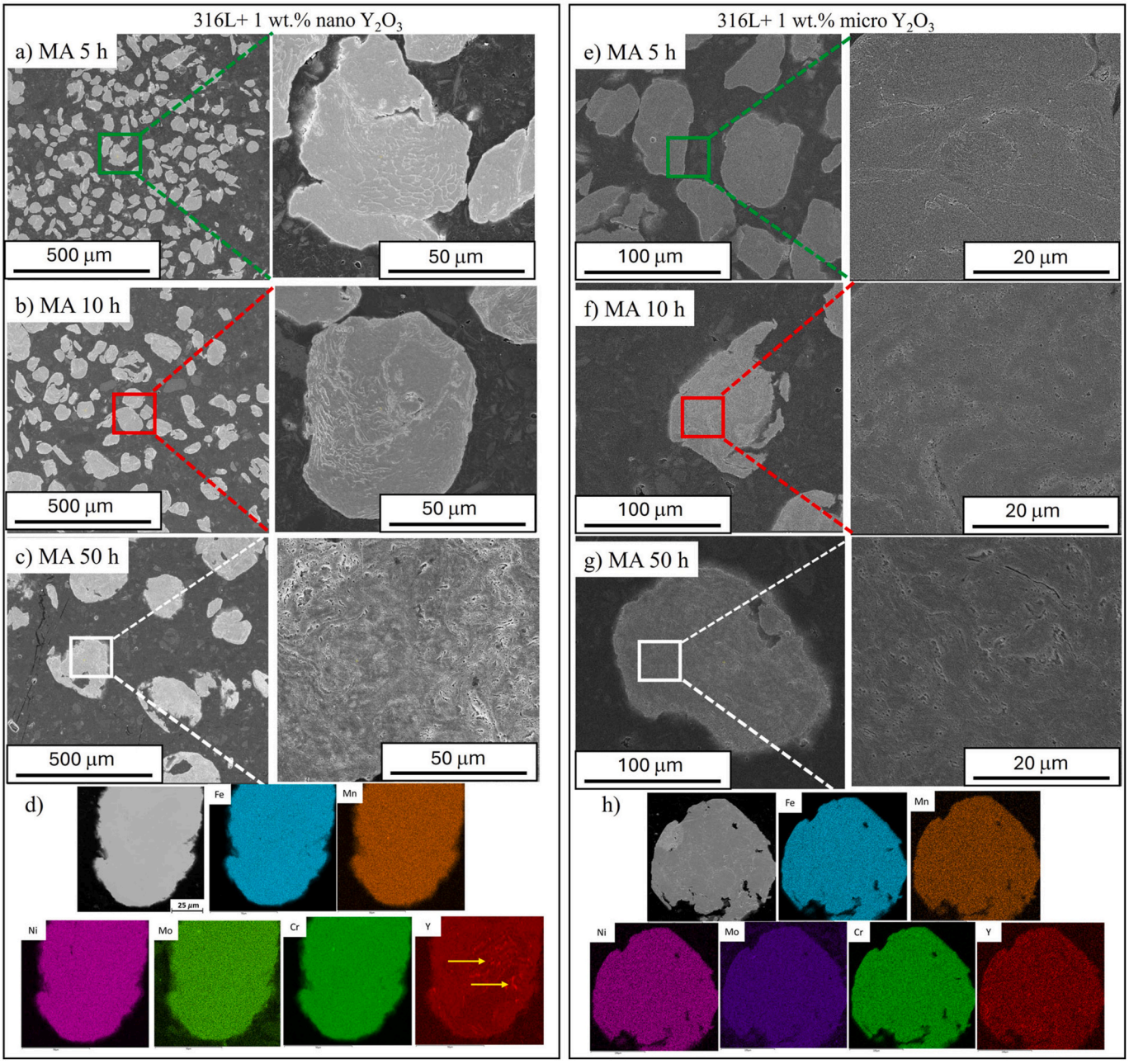


**Fig. 2.** Powders microstructure obtained after mechanical alloying of 316L with 1 wt% of nano-sized $Y_2O_3$ for: a) 5 h, b) 10 h, and c) 50 h, and of 316L with 1 wt% of micro-sized $Y_2O_3$ for: e) 5 f) 10 h and g) 50 h. EDX analyses for the powder after 50 h of MA for 316L with 1 wt% of nano- and micro-sized $Y_2O_3$ are shown in panel d and g, respectively.

present in the form of banded, Y-enriched agglomerates formed by cold-welded platelets (marked by the yellow arrows). This phenomenon is attributed to repeated impacts from the milling balls, which induce intense deformation of the smaller particles, followed by their cold welding into layered morphologies. Such structures are prominent after extended milling times, although the outlines of the original particles can still be distinguished. Within the particles, individual grains can be observed, reaching sizes of several tens of microns. Fig. 2e–g presents the cross-sectional microstructures of 316L with 1 wt% micro-sized $Y_2O_3$ after various MA durations. The particles exhibit sharp-edged morphologies, characteristic of MA processing, where repeated cold welding and plastic deformation occur. Fragments of the smaller, original particles are visible within the larger agglomerates, indicating their coalescence through cold welding. Despite this, the elemental distribution appears homogeneous across the agglomerates with the exemption of Y, which forms layered structures as in previous case (Fig. 2h).

### 3.2. Microstructural characterization

The samples fabricated by PPS exhibited high densification levels

**Table 2**
Density measurements of the reference 316L, and 316L with 1 wt % of nano- and micro-sized $Y_2O_3$ additions fabricated via PPS.

| Material | 316L | 316L+1 wt% nano $Y_2O_3$ | | | 316L+1 wt% micro $Y_2O_3$ | | |
|---|---|---|---|---|---|---|---|
| Time of MA (h) | none | 5 | 10 | 50 | 5 | 10 | 50 |
| Density (g/cm$^3$) | 7.85 | 7.90 | 7.90 | 7.87 | 7.90 | 7.86 | 7.64 |
| % of TD | 98.1 | 99.3 | 99.3 | 99.0 | 99.3 | 98.8 | 96.1 |

*TD – theoretical density.

(Table 2). The reference 316L sample, processed without MA, reached 98.1% of its theoretical density. Even higher relative densities, exceeding 99%, were achieved for ODS steels reinforced with 1 wt% of nano-sized $Y_2O_3$, regardless of MA time. A slight decrease in density was observed only for the sample subjected to the longest milling time (50 h). In contrast, the samples containing 1 wt % of micro-sized $Y_2O_3$ showed a more pronounced sensitivity to MA. While high densification was maintained after shorter MA times (5–10 h), the relative density dropped significantly to 96.1% after 50 h of milling. This effect is attributed to PSD: the samples fabricated by PPS exhibited high densification levels (Table 1). The reference 316L sample, processed without MA, reached 98.1% of its theoretical density (TD). Even higher relative densities, exceeding 99%, were achieved for ODS steels reinforced with 1 wt% of nano-sized $Y_2O_3$, regardless of MA time. A slight decrease in density was observed only for the sample subjected to the longest milling time (50 h). In contrast, the samples containing 1 wt% of micro-sized $Y_2O_3$ showed a more pronounced sensitivity to MA. While high densification was maintained after shorter MA times (5–10 h), the relative density dropped significantly to 96.1% after 50 h of milling. This effect is primarily attributed to the PSD: a wider PSD improves powder flowability, as smaller particles fill the voids between larger ones. The SEM images with the corresponding PSD are given in Supplementary Materials (Fig. S2 and Fig.S3).

For the as-received 316L powder, the PSD was narrow, with D10/D50/D90 = 26/30/34 μm and $D_{avg}$ = 30 μm, whereas after 5 h of MA with 1 wt% nano- and micro-sized $Y_2O_3$, the PSDs broadened markedly to 34/63/172 μm ($D_{avg}$ = 83 μm) and 26/44/77 μm ($D_{avg}$ = 50 μm), respectively. Such broad, quasi-bimodal distributions promote high tap and green densities because fine particles can occupy the interstices between coarser ones. In combination with surface activation during MA, this facilitates almost complete pore closure during PPS and explains the >99%TD reached by the ODS steels after 5–10 h of MA. With increasing MA duration, the powders became much coarser and more irregular in shape (Figs. 1 and 2). After 50 h of MA both nano- and micro-doped blends exhibited very large, flake-like agglomerates with D10/D50/D90 ≈ 192/266/381 μm and 194/257/375 μm, respectively. These strongly work-hardened platelets pack less efficiently, tend to trap pores between overlapping flakes and undissolved $Y_2O_3$ agglomerates (Fig. 7), and cannot undergo sufficient plastic accommodation during the short PPS cycle. As a result, the relative density decreases slightly for the nano-doped steel and more markedly for the micro-doped steel (down to 96.1% TD) after 50 h of MA, despite the wide PSD of the corresponding powders.

A typical coarse-grained microstructure was observed in the reference 316L stainless steel (Fig. 3a), with an average grain size of approx. 100 μm and random orientations (Fig. 3b). Pores, marked with red arrows, are also visible in Fig. 3a. In the sintered materials, bimodal microstructures are observed, regardless of MA duration or $Y_2O_3$ particle size (Fig. 3d–f and Fig. 3m–o). Both the average grain size ($d_{avg}$) and the fraction of coarse and small grains are strongly affected by milling time. For the materials with nano-sized $Y_2O_3$, the largest $d_{avg}$ of 4.5 μm was measured after 5 h of MA (Fig. 3g), decreasing to 2.5 μm after 10 h (Fig. 3h) and further refining to approximately 1.2 μm after 50 h (Fig. 3i). A similar grain refinement trend was found for the micro-sized $Y_2O_3$ additions with $d_{avg}$ decreasing from 4.4 μm after 5 h (Fig. 3p) to 3.2 μm after 10 h (Fig. 3r) and reaching the 1.4 μm after 50 h (Fig. 3s). In all cases, the grains exhibited random crystallographic orientations, with no evidence of a preferred texture.

The proportion of fine to coarse grains also evolved with MA duration, as illustrated by the grain size distribution curves in Fig. 4. MA significantly refined the grain size compared with the reference steel, and the fraction of the smallest grains increased with milling time. After 5 h of MA, 82% of grains in the materials with nano-sized $Y_2O_3$ additions were smaller than 5 μm, with a similar fraction observed for the micro-sized $Y_2O_3$ additions. After 10 h, the difference between the two became more pronounced, with 92% and 87% of grains below 5 μm for nano- and micro-sized $Y_2O_3$, respectively. The highest fractions of fine grains were achieved after 50 h of MA duration, reaching 98% for nano-sized and 96% for micro-sized $Y_2O_3$ additions.

Fig. 3k–m and Fig. 3u–w present also GND maps obtained based on the EBSD measurements. The highest accumulation of GNDs takes place in the vicinity of the grain boundaries and fine-grained regions, while significantly lower GND density is observed in the central part of coarser grains. The calculated average GND density of the reference 316L steel was $2.1 \times 10^{13}$ $m^{-2}$. All samples containing nano- or micro-sized $Y_2O_3$ showed higher accumulation of GNDs. The GND density gradually increased for longer MA times and reached values of: 3.7, 4.8 and $5.5 \times 10^{13}$ $m^{-2}$ for materials with nano-sized $Y_2O_3$ after 5, 10 and 50 h of MA, respectively, and 3.2, 3.8 and $4.9 \times 10^{13}$ $m^{-2}$ for materials with micro-sized $Y_2O_3$, respectively.

TEM observations confirmed that the microstructure of the sintered materials was heterogeneous, consisting of both small, equiaxed grains and regions with significantly larger grain sizes (Fig. 5). This is consistent with the EBSD results presented in Fig. 3. TEM also revealed the presence of round black particles, primarily located within the fine-grained regions (highlighted by the yellow arrows in Fig. 5a and b). EDX analysis identified these particles as being rich in Y and O, confirming that they are $Y_2O_3$ (Fig. 5c), a finding further supported by XRD analysis (Fig. 6). No carbides were detected via XRD and EDX, which was corroborated by combustion analysis showing carbon contamination below 0.01 wt% in all materials. However, a fraction of $Y_2O_3$ remained in the form of undissolved agglomerates, even after the longest MA duration, for both micro- and nano-sized additions. The spatial distribution of these undissolved remnants is illustrated in Fig. 7. They are located mainly at grain boundaries, which is clearly visible in the coarse-grained regions after 5 h of MA. After longer MA times (10 h, 50 h), the fraction of the fine grains increased while the $Y_2O_3$ agglomerates were continuously fragmented and thus, their spatial distribution became more uniform. Nevertheless, these agglomerates are expected to reduce the plasticity of the ODS alloys due to their brittle nature [43].

### 3.3. Mechanical properties

The tensile properties of the investigated materials are shown in Fig. 8 and in Table 3. The reference 316L stainless steel exhibited the highest A reaching 49 % but also the lowest UTS of 533 ± 6 MPa. MA significantly influenced the mechanical performance of the ODS steels, regardless of $Y_2O_3$ particle size. The longest MA duration (50 h) produced the highest strength but the lowest ductility. The UTS values for the 50 h MA samples were 918 ± 5 MPa (nano-sized $Y_2O_3$) and 938 ± 9 MPa (micro-sized $Y_2O_3$), accompanied by elongations of only 4% and 3%, respectively. In contrast, samples milled for 5 h showed the highest ductility, with elongations of approximately 14%, but exhibited the lowest strength. Their UTS values were 519 ± 37 MPa (nano-sized $Y_2O_3$) and 544 ± 13 MPa (micro-sized $Y_2O_3$). The corresponding YS were 364 ± 8 MPa and 365 ± 4 MPa, respectively.

Fig. 9 illustrates the fracture surface morphologies of 316L stainless steel and the austenitic ODS steels. The reference 316L sample exhibited a typical ductile fracture with noticeable porosity and a mixture of large and fine voids (Fig. 9a). Samples sintered after 5 h of MA with nano- and micro-sized $Y_2O_3$ additions (Fig. 9b and e) showed a finer ductile fracture morphology, characterized by shallower dimples and a smaller area fraction of tearing edges compared with the other ODS materials. In contrast, the samples processed for 50 h (Fig. 9d and g) exhibited a clear reduction in ductility, as evidenced by an increased fraction of tearing edges and the absence of deep, uniform dimples. These features less pronounced in the 5 h and 10 h milled samples (Fig. 9c and f). Notably, the most ductile ODS materials, those milled for 5 h with either nano- or micro-sized $Y_2O_3$, displayed a mixed fracture mode, combining features of ductile fracture and quasi-cleavage features.

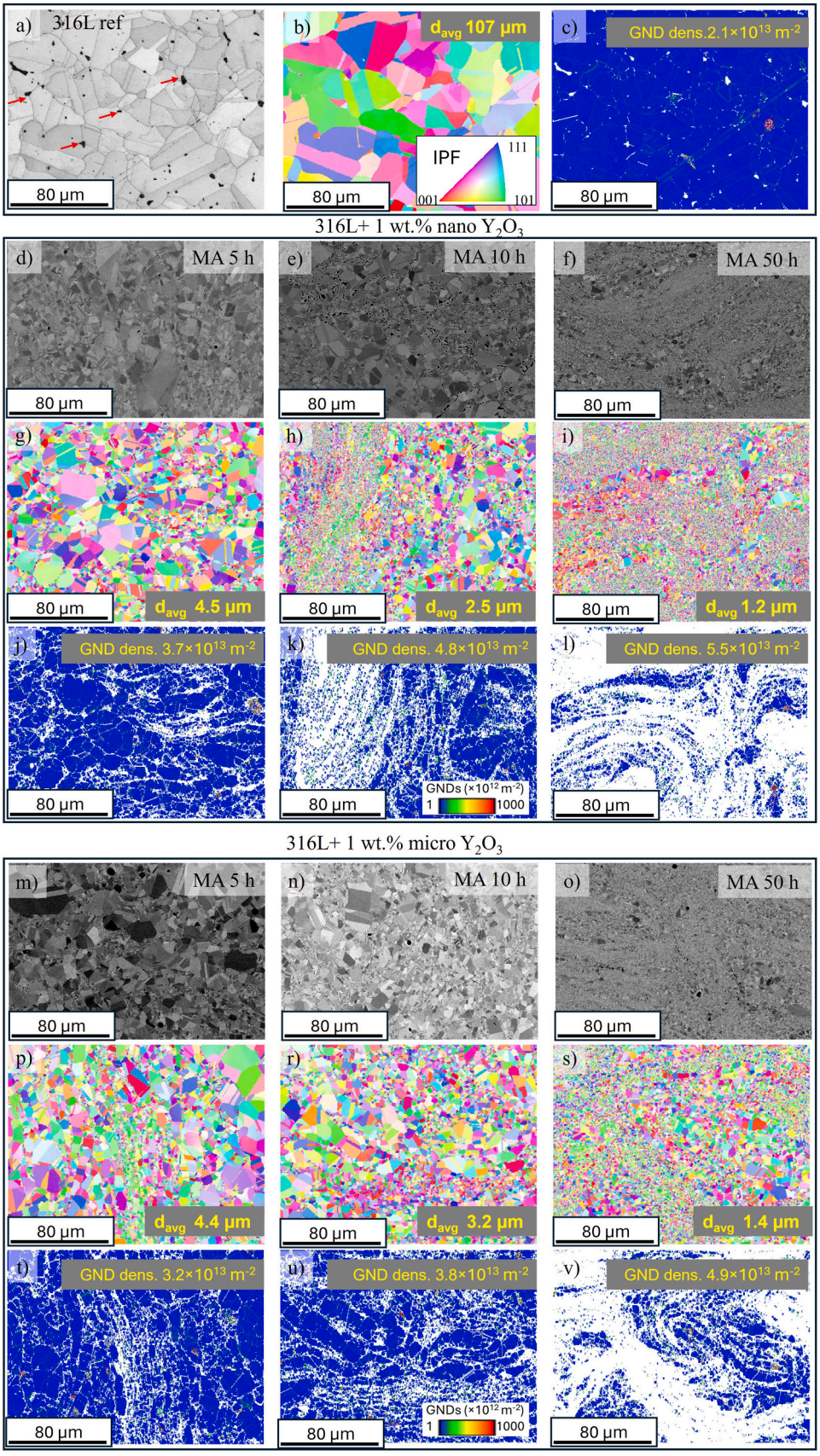


(caption on next page)

**Fig. 3.** Microstructure characterization of the reference 316L: a) SEM microstructure, b) inverse pole figure (IPF) map and c) geometrical necessary dislocations (GND) density map. The 316L with nano-sized $Y_2O_3$ produced by 5 h, 10 h and 50 h of MA and sintering using PPS: (d-f) SEM microstructures, (g-i) inverse pole figure (IPF) maps, (j-l) geometrical necessary dislocations (GND) density maps, and 316L with micro-sized $Y_2O_3$ produced by 5 h, 10 h and 50 h of MA and sintering using PPS: (n-p) SEM microstructures, (r-t) inverse pole figure (IPF) maps and (u-w) geometrical necessary dislocations (GND) density maps. Color-coded legends for IPF and GNDs are given in the right upper corner; $d_{avg}$ - average grain size, GND den. – GND average density. Data obtained from the plane perpendicular to the sintering direction.

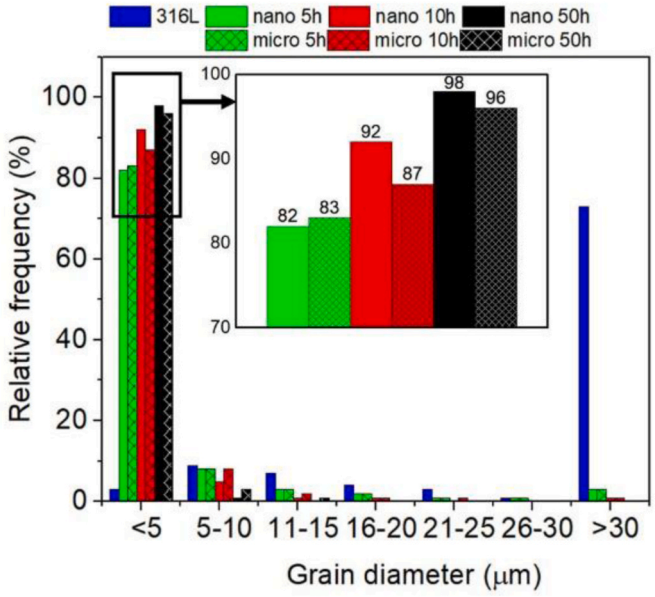


**Fig. 4.** Grain size distribution calculated for the reference 316L, and the 316L with nano- and micro-sized $Y_2O_3$ addition after 5 h, 10 h and 50 h of MA and sintered using PPS.

### 3.4. Corrosion performance

Our results clearly demonstrate that MA duration is the predominant factor influencing the corrosion rate of the investigated materials after salt spray exposure. As shown in Fig. 10, the lowest corrosion rate, approx. 0.7 ± 0.01 μm/year, was measured for samples sintered after 5 h of MA. This value is nearly half that of the reference 316L stainless steel, which exhibited a corrosion rate of around 1.4 ± 0.00 μm/year. Surprisingly, the corrosion rates of the reference material and the ODS steels processed for 10 h of MA were nearly identical. In contrast, the highest corrosion rates were recorded for the samples processed for 50 h. Specifically, ODS steel with nano- and micro-sized $Y_2O_3$ additions reached corrosion rates of 2.1 ± 0.69 μm/year and 3.0 ± 0.33 μm/year, respectively. The results indicate that prolonged MA not only worsens corrosion resistance but also amplifies the difference in performance between nano- and micro-sized $Y_2O_3$ additions.

Figs. 11 and 12 show the surface morphologies after chemical removal of the corrosion products formed during salt spray exposure. Distinct differences in corrosion patterns were observed between the reference specimen and the samples sintered after various MA durations. The observed discrepancy may be attributed to the porosity of the reference sample, likely caused by incomplete optimization during PPS processing. All samples exhibited localized corrosion in the form of deep valleys of varying size and random distribution. The most extensive but shallowest damages on the surface damage was observed in the samples processed for 5 h of MA, for both nano- and micro-sized $Y_2O_3$ additions (Figs. 11b and 12a). In contrast, the deepest corrosion damage occurred in samples of MA for 10 h (Figs. 11d and 12b), while the samples processed for 50 h displayed the most widespread surface attack (Figs. 11d and 12c). Overall, the severity of corrosion damage increased with MA duration. This trend was corroborated by surface roughness measurements ($S_a$), which increased progressively with milling time: 31 ± 24, 41 ± 22, and 99 ± 67 nm for nano-sized $Y_2O_3$ materials after 5, 10, and 50 h of MA, respectively; and 26 ± 5, 94 ± 30, and 93 ± 25 nm for the micro-sized $Y_2O_3$ materials.

## 4. Discussion

### 4.1. Mechanical alloying parameters and microstructure formation

In contrast to Mayer et al. [44], our results unambiguously demonstrate that nano-precipitates of $Y_2O_3$ formed in the processed materials, regardless of whether nano-sized or micro-sized yttria was used. While the authors highlighted a strong temperature-driven refinement of $Y_2O_3$ during MA, our findings on PPS-316L ODS steels instead show that milling duration, not initial yttria size, governs the resulting nano-oxide formation. The results of our work show that the predominant role in microstructure formation of austenitic ODS steels has MA timing, not yttria size itself. The powder mixtures of 316L with 1 wt% of $Y_2O_3$ addition, regardless of particle size, underwent plastic deformation during MA due to the ball-particle-ball and ball-to-wall collisions. This led to the formation of flattened particles, and with increasing MA duration, particles with larger perimeters were produced. This observation contrasts with the results of Wang et al. [45], who investigated 304L austenitic ODS steels containing both yttria and Ti, whereas in our work only yttria was introduced into the powder blend. In both studies no PCA agent was used during milling. In Ti-containing ODS systems, the addition of Ti is well known to suppress particle and grain coarsening. Because Ti is far more reactive than yttria and dissolves more readily during mechanical alloying, it accelerates the alloying process and promotes the formation of fine Y–Ti–O complexes. At the same time, this enhanced reactivity increases the degree of work hardening in the powder particles. The growing internal strain reduces powder ductility during milling, ultimately causing fatigue cracking and fragmentation of the increasingly brittle particles. A similar behaviour was reported by Kumar et al. [46], who also observed extensive particle refinement resulting from severe work hardening in Ti-bearing mechanically alloyed powders. Nevertheless, alloying of the powders was achieved in the present study. The irregular morphologies of the powders observed after the shortest MA duration are consistent with those reported by Ninawe et al. [47] after 20 h of milling of Fe–16Cr–16Ni–1.5 W–0.21Ti–0.3$Y_2O_3$ wt.%, and by Suresh [48] after 4 h of milling Fe-16.8Cr–22Ni–2W-2.4Mo-1.5Mn-0.62Si-0.15La-0.2Ti + 0.35 wt % of $Y_2O_3$. These discrepancies clearly indicate that the final shape and size of austenitic ODS powders are strongly influenced by both the chemical composition of the blend and the parameters of the MA process. Consequently, the MA parameters must be individually optimized for each specific austenitic ODS composition, making the preparation of suitable powders a time-consuming and iterative procedure.

Short-time MA has already been investigated for ferritic steels, and consistent with our finding, it does not lead to the full dissolution of $Y_2O_3$ within the steel matrix [49,50]. The presence of undissolved $Y_2O_3$ remnants is known to influence both mechanical and corrosion properties. It should also be noted that yttria agglomeration during mechanical alloying and subsequent sintering affects the resulting properties of the materials. A considerable difference in the mechanical properties is observed between steels with nano- and micro-sized yttria additions after 10 h of mechanical alloying. Since the density of the corresponding material was also reduced, we suppose that this effect is related to the agglomeration of the ceramic filler, which is unfortunately

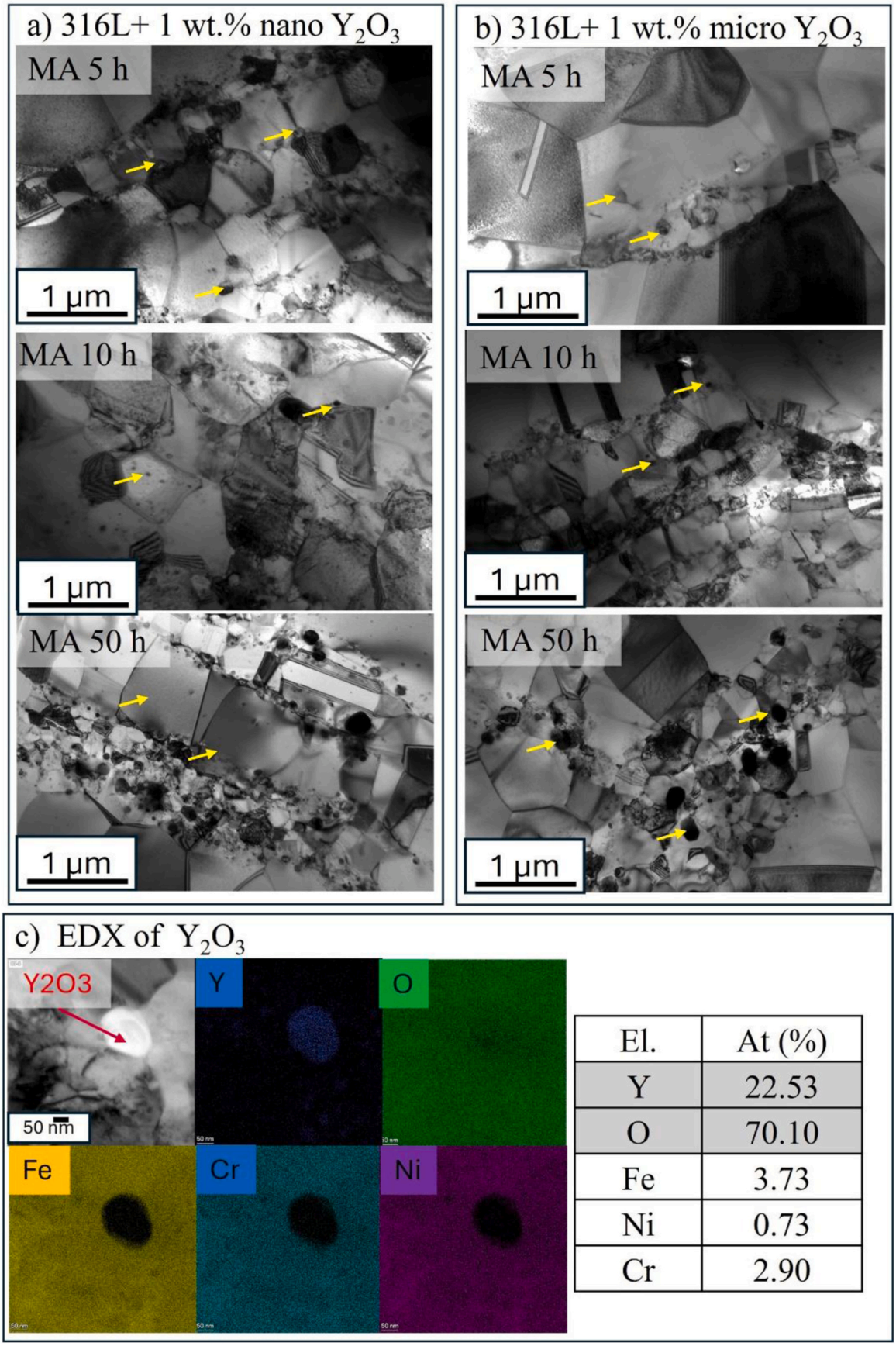


| El. | At (%) |
|---|---|
| Y | 22.53 |
| O | 70.10 |
| Fe | 3.73 |
| Ni | 0.73 |
| Cr | 2.90 |

**Fig. 5.** TEM images in bright field obtained for the 316L with 1 wt% of $Y_2O_3$ addition after 5 h, 10 h and 50 h of MA: a) nano-sized $Y_2O_3$ b) micro-sized $Y_2O_3$ c) EDX analysis of the representative $Y_2O_3$ particles.

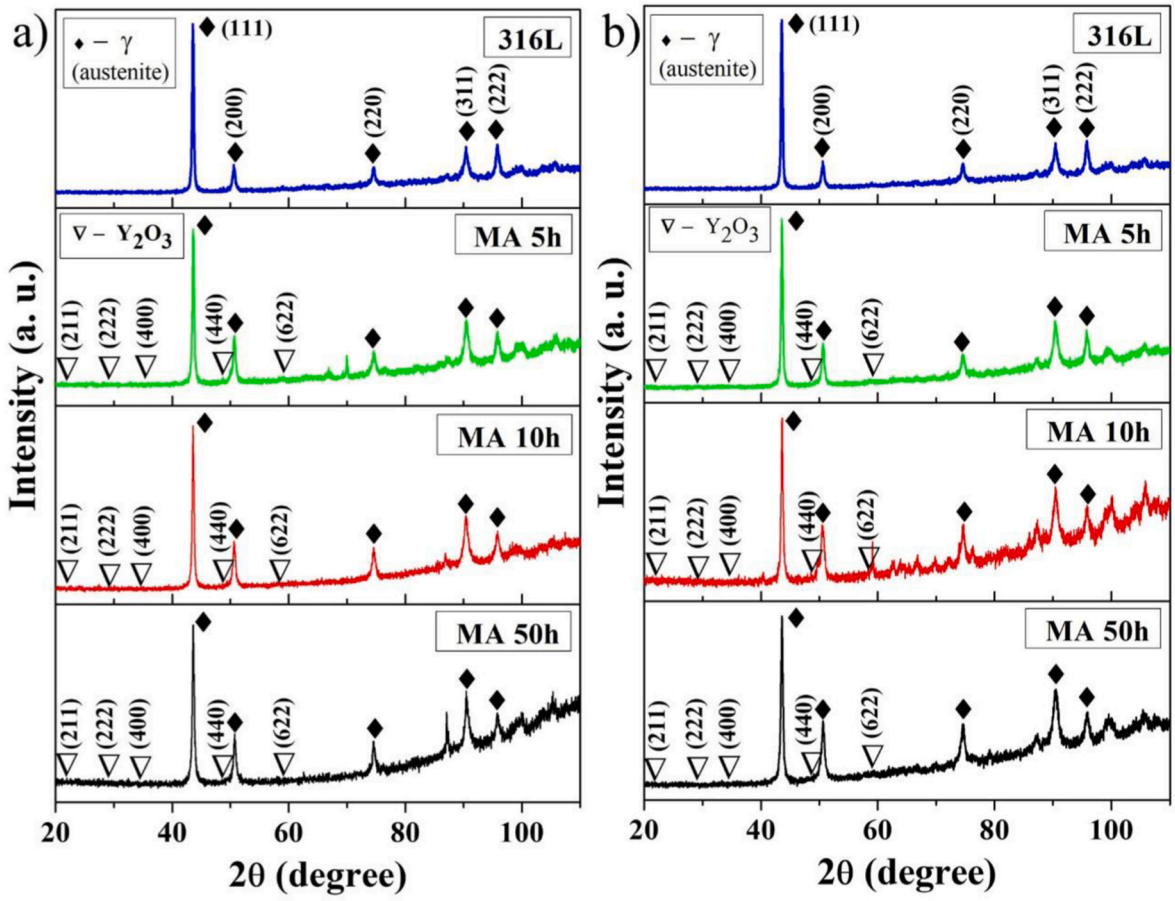


**Fig. 6.** Phase identification of the 316L and 316L with 1% wt. addition of a) nano-sized $Y_2O_3$ and b) micro-sized $Y_2O_3$ fabricated using PPS (ICSD for $Y_2O_3$ 86815).

difficult to avoid during processing.

The bimodal microstructure observed in the present study is a typical feature of ODS steels sintered using plasma-assisted method. Similar microstructure have been reported for both ferritic ODS steels [51–54] and austenitic ODS steels [33]. Gräning et al. [33] showed that such bimodality persists even when finer starting powders are used, indicating that it is an inherent consequence of the MA process. This observation supports the conclusion that bimodal microstructure formation is primarily driven by strain heterogeneities introduced into the powder particles during MA, as previously demonstrated by García-Rodríguez et al. [55] and Boulnat et al. [54]. Moreover, the dislocations observed within the fine grains suggest that discontinuous recrystallization occurred during processing. This mechanism typically results from an inhomogeneous deformation microstructure [56], with nucleation preferentially taking place at sites of high local misorientation, which is consistent with our EBSD observations.

### 4.2. Mechanical properties

The calculated mechanical properties (Table 4), engineering stress–strain curves (Fig. 8) and fractographic analyses (Fig. 9) indicate that the mechanical performance of the investigated ODS steels was governed primarily by the MA conditions, rather than by the size of the $Y_2O_3$ addition. To understand more deeply the correlation between the applied MA conditions and the obtained different microstructures and yield strength values, the contributions of various strengthening mechanisms were quantified, as summarized in Table 3. According to a theory proposed by Hansen [57], the yield strength can be theoretically calculated as the sum of lattice friction ($\sigma_0$), solid solution ($\sigma_{ss}$), dislocation ($\sigma_d$), grain boundary ($\sigma_{gb}$) and particles ($\sigma_p$) strengthening. It has been shown that a linear summation of all contributions may lead to overestimation of the theoretically calculated yield strength values of ODS steels. Thus, a Pythagorean superposition of the contributions from dislocations and particles was suggested by several authors [58–60]. Kamikawa et al. [59] showed that small spacing of dislocations and precipitates are comparable and both are acting as short range obstacles. Thus, their strengthening contributions can be used together in the following formula:

$$\sigma = \sigma_0 + \sigma_{ss} + \sigma_{gb} + \sqrt{{\sigma_d}^2 + {\sigma_p}^2} \quad (2)$$

The lattice friction can be defined as the Peierls-Nabarro stress equal to 2 x $10^{-4}$ G [61], where G is the shear modulus reported as G = 86.2 GPa for austenitic stainless steel [62]. Therefore, the lattice friction for 316L steel can be estimated as 17 MPa.

The solid solution strengthening for stainless steels can be expressed by Ref. [63]:

$$\sigma_{ss} = \sum k_i c_i \quad (3)$$

where $k_i$ represents the strengthening coefficient of i-th alloying element in the matrix and $c_i$ is the concentration of the alloying element in wt%. Based on the studies of Yusuf et al. [64], Eliasson and Sandström [65], the following strengthening coefficient were used in the calculation: $k_{Cr}$ = 1, $k_{Ni}$ = 5, $k_{Mo}$ = 19.5, $k_{Mn}$ = −1.5, $k_C$ = 219.6 and $k_{Si}$ = 8.7 MPa/wt %. Considering the chemical composition given in Table 1, the solid solution strengthening of the investigated 316L steel was estimated at the level of about 139 MPa, which is in the range of values obtained by Yusuf et al. (115.4 MPa) [64] and Chen et al. (169 MPa) [66].

Whereas the same lattice friction and solid solution strengthening can be assumed in the calculation for each sample, the main differences

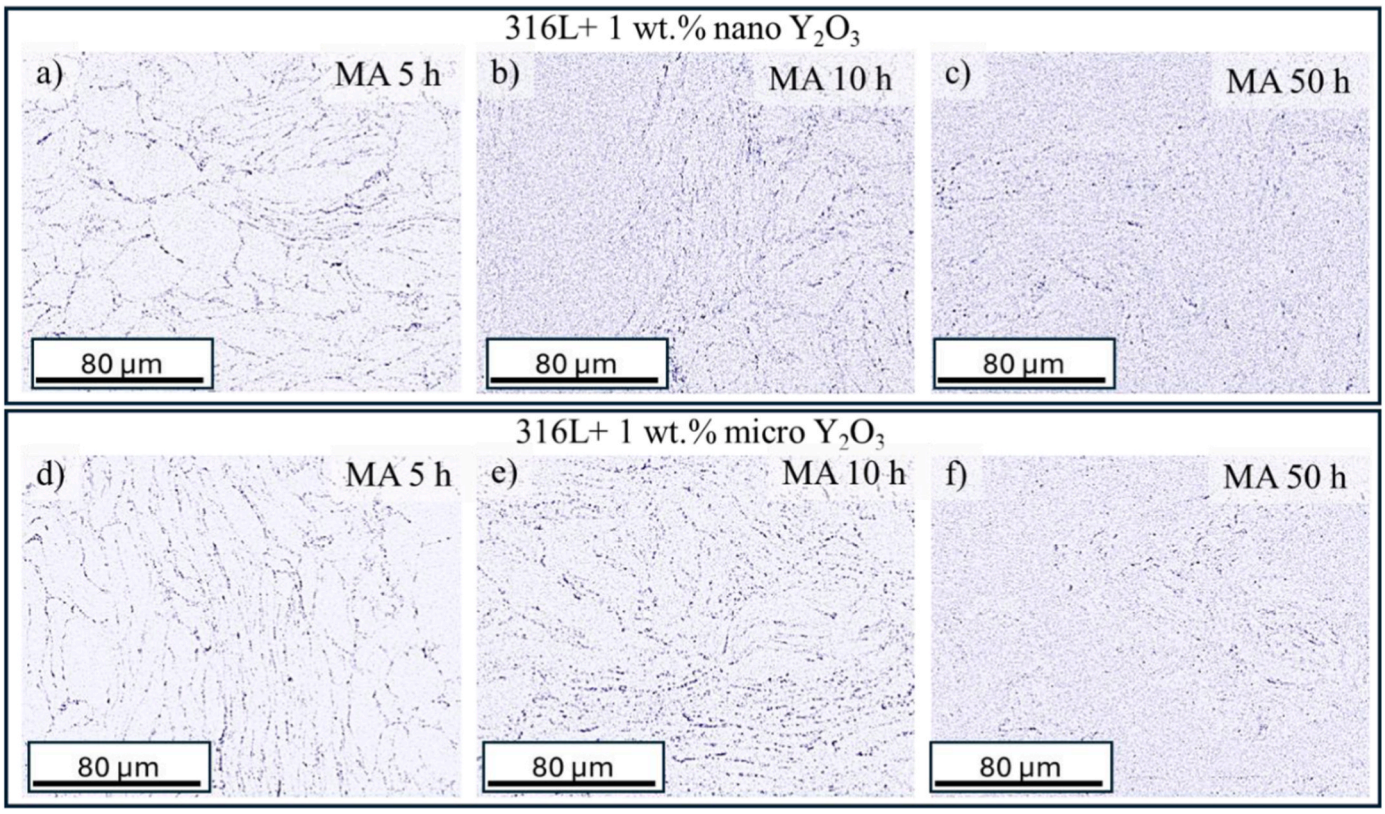


**Fig. 7.** Distribution of $Y_2O_3$ within 316L ODS steels with 1% wt. nano-sized $Y_2O_3$ after mechanical alloying for a) 5h, b) 10 h, c) 50 h, and micro-sized $Y_2O_3$ after mechanical alloying for d) 5h, e) 10 h,f) 50 h, and subsequent PPS based on EBSD measurements.

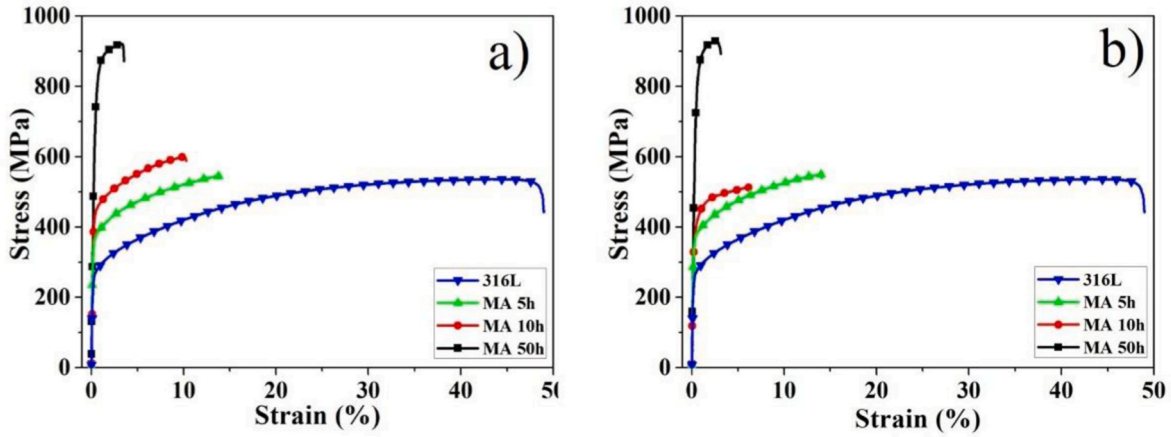


**Fig. 8.** Stress-strain curves and the calculated YS, UTS and A obtained for 316L with the addition of 1 wt% of a) nano-sized $Y_2O_3$ and b) micro-sized $Y_2O_3$, sintered using PPS.

can be expected in the grain boundary strengthening due to the various grain size distributions obtained after different MA time. According to the well-known Hall-Petch relationship, the grain boundary strengthening can be calculated from the following formula [67,68]:

$$\sigma_{gb} = k_{HP} d^{-0.5} \quad (4)$$

where: d is the average grain size and $k_{HP}$ is the constant from the Hall-Petch relation. It has been reported for the 316L steel that the Hall-Petch coefficient may vary depending on the investigated grain size regime [69–71]. Nevertheless, Astafurov et al. [71] has recently proved that the Hall-Petch coefficient of $k_{HP} = 327$ MPa $\mu m^{0.5}$ provides a good agreement of the results for the 316 stainless steel in the grain size ranging from 2.8 to 73 µm. Moreover, it has been shown that a volume-weighted grain size gives a more reliable grain boundary strengthening for materials exhibiting a bimodal grain size distribution [72,73]. Therefore, the volume-weighted mean grain size $D_v$ (formulated as $(\Sigma V_i/d_i)/V$ where $V_i$ is the volume of grains with the size of $d_i$ and V is the total analyzed volume) was estimated for each sample with the $Y_2O_3$ addition and used in the calculations of grain boundary strengthening contribution. In the case of the 316L steel modified with the nano-sized $Y_2O_3$, the average volume-weighted grain size $D_v$ of 9.5, 5.0 and 2.2 µm after 5, 10 and 50 h of MA, respectively, resulted in the strengthening contribution of about 106, 146 and 222 MPa, respectively. A similar trend was observed for the 316L steel with the micro-sized $Y_2O_3$, i.e. $D_v$ of 9.1, 6.7

**Table 3**
Characteristic parameters calculated based on the tensile tests of the reference 316L, and 316L with 1 wt % of nano- and micro-sized $Y_2O_3$ additions fabricated via PPS (YS – yield strenght, UTS – ultimate tensile strenght, A - elongation at fracture).

| | YS (MPa) | UTS (MPa) | A (%) | YS (MPa) | UTS (MPa) | A (%) |
|---|---|---|---|---|---|---|
| 316L | 261 ± 3 | 533 ± 6 | 49 ± 1 | - | - | - |
| MA time | 316L+1 wt% nano-sized $Y_2O_3$ | | | 316L+1 wt% micro-sized $Y_2O_3$ | | |
| 5 h | 364 ± 8 | 519 ± 37 | 14 ± 4 | 365 ± 4 | 544 ± 13 | 14 ± 3 |
| 10 h | 444 ± 4 | 602 ± 26 | 11 ± 3 | 392 ± 18 | 509 ± 15 | 6 ± 1 |
| 50 h | 776 ± 17 | 918 ± 9 | 4 ± 1 | 793 ± 10 | 938 ± 9 | 3 ± 1 |

and 2.5 μm after 5, 10 and 50 h of MA provided the grain boundary strengthening of about 108, 126 and 208 MPa, respectively.

Another microstructural feature varying with the applied MA conditions was the dislocation density as presented in the GND maps (Fig. 3). According to the Taylor theory, the dislocation strengthening can be described as [74]:

$$\sigma_d = M\alpha bG\rho^{0.5} \quad (5)$$

where: ρ is the dislocation density, M is the Taylor factor and a value of M = 3.06 can be taken for a weak textured material [75], α is a constant related to the dislocation type, typically given as 0.24 for FCC metals [76], and b is the Burger's vector of b = 0.248 nm for the austenitic steel [58]. Considering the above mentioned constants and the dislocation density presented in Fig. 3, the dislocation strengthening of the reference material was around 71 MPa. It gradually increased for longer MA time reaching values of: 95, 109 and 117 MPa for the 316L steel with nano-sized $Y_2O_3$, and 89, 97 and 110 MPa for the 316L steel with micro-sized $Y_2O_3$ after 5, 10 and 50 h of MA, respectively.

Due to the heterogeneous distribution of $Y_2O_3$ and the presence of numerous $Y_2O_3$ agglomerates (as presented in Fig. 7), it was not possible to precisely calculated the last strengthening contribution from $Y_2O_3$ particles ($\sigma_p$). Nevertheless, it was estimated based on the difference between the rest of strengthening contributions (Table 1) and the experimentally determined yield strength values (Table 2). The reference 316L steel exhibited the lowest YS but the highest elongation to failure, consistent with its coarse, fully recrystallized grain structure [54]. The sum of calculated strengthening contributions from lattice friction, solid solution, grain boundaries and dislocations gives a value of 259 MPa for the reference material. It is very close to the experimentally determined YS of 261 MPa what supports a good accuracy of the assumed theoretical calculations and constants. In agreement with the findings of Wang et al. [45] and Garcia-Junceda et al. [77], the ODS steels with nano- and micro-sized $Y_2O_3$ demonstrated markedly higher strength than the reference 316L steel. In the literature references, this strength enhancement is mainly attributed to the uniform dispersion of oxide particles, which impede dislocation motion through the Orowan

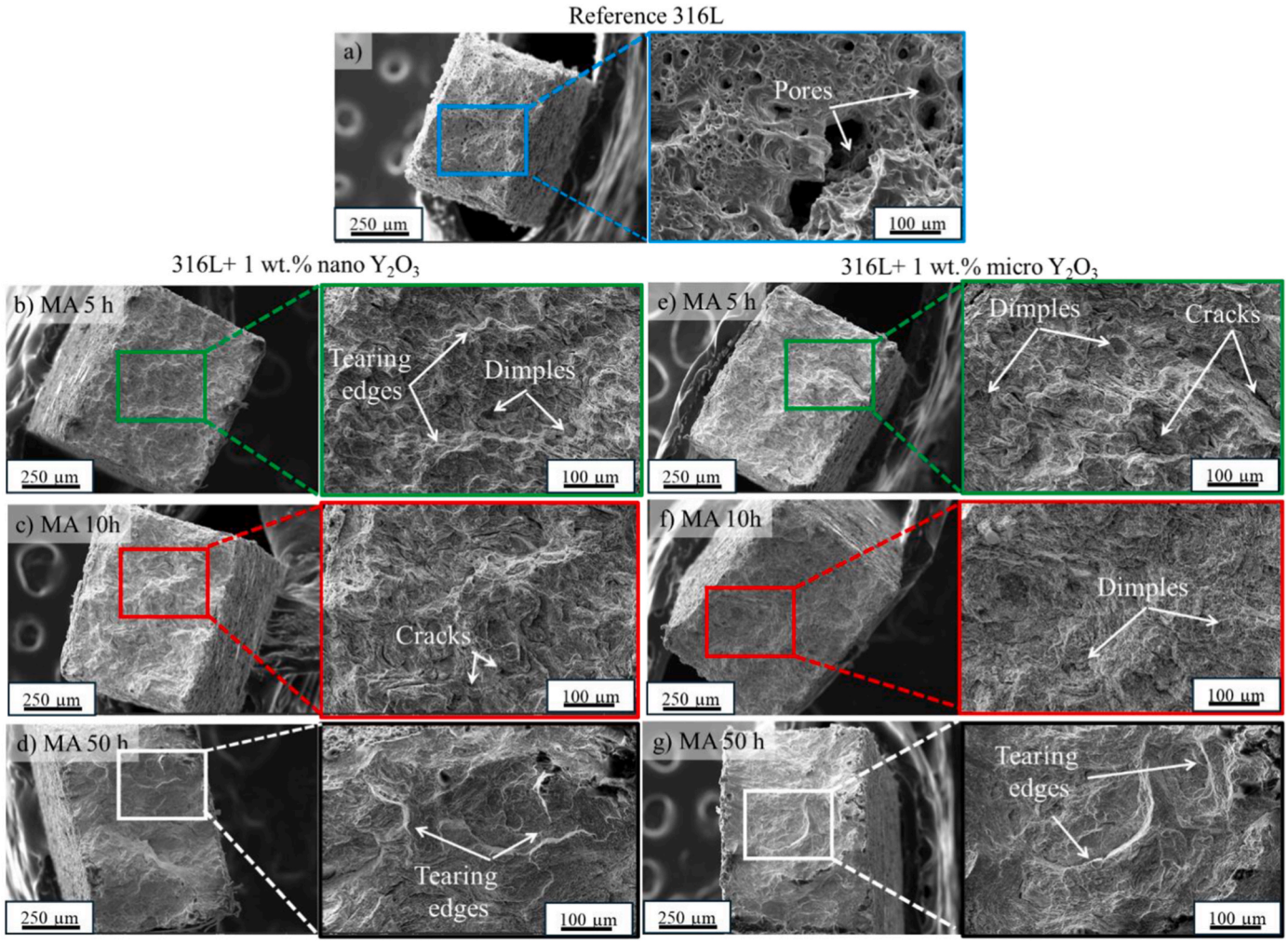


**Fig. 9.** Fractography of the samples after tensile tests: a) reference 316L stainless steel, (b-d) 316L with the addition of 1 wt% of nano-sized $Y_2O_3$ and (e-f) 316L with the addition of 1 wt% of micro-sized $Y_2O_3$ mechanically alloyed for 5, 10 and 50 h, respectively, and sintered using PPS.

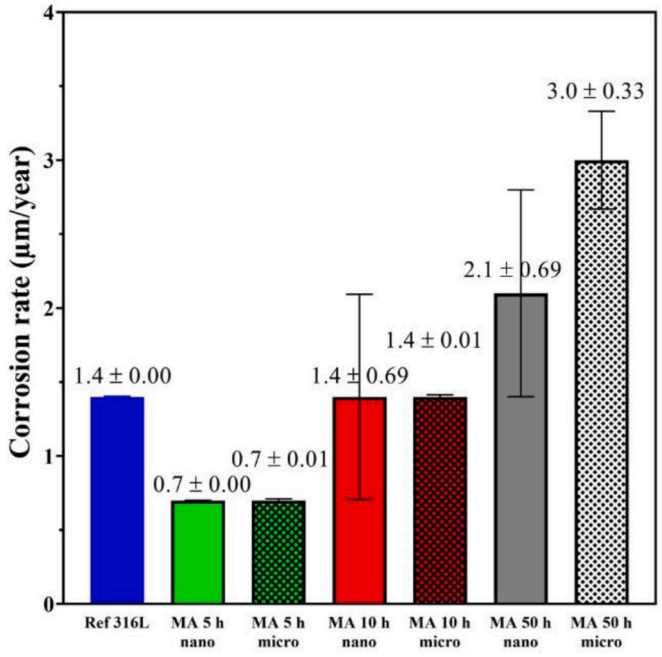


**Fig. 10.** Corrosion rate calculated based on the mass loss method for the investigated materials: reference 316L stainless steel, 316L with the addition of 1 wt% of nano- and micro-sized $Y_2O_3$ after 5 h, 10 h and 50 h of MA sintered using PPS.

bypass mechanism [67]. If we subtract the calculated strengthening contributions from the experimental YS value using Eq. (2), we get the following particles strengthening contribution ($\sigma_p$): 36, 92 and 380 MPa for the 316L steel with nano-sized $Y_2O_3$, and 46, 52 and 415 MPa for the 316L steel with micro-sized $Y_2O_3$ after 5, 10 and 50 h of MA, respectively. It clearly shows that the particles strengthening becomes dominant strengthening mechanism after 50 h of MA, whereas for shorter milling times (5 and 10 h) the strengthening is provided mainly by the grain boundaries and the dislocations. It is consistent with the microstructural observations presented in Figs. 3 and 7. A substantial contribution from $Y_2O_3$ particle strengthening is not expected after 5 and 10 h of MA, since the particles are predominantly located at grain boundaries and are not homogeneously distributed within the matrix, particularly inside the grains. When increasing milling time to 50 h, a significantly improved homogenization of $Y_2O_3$ particles is observed, including their presence within the grains. This leads to a pronounced increase in strength, with the additional strengthening contribution attributable to oxide dispersion being roughly estimated at ~400 MPa, which is close to values of 420-530 MPa reported by Chauhan et al. [58] for different ODS steels. It should be also noted that this strengthening effect is accompanied by a drastic reduction in ductility (Table 2), as a higher density of intragranular $Y_2O_3$ particles shortens the dislocation mean free path, thereby limiting plastic deformation. In general, the current results clearly show that the presence of $Y_2O_3$ agglomerates at grain boundaries (Fig. 7) leads to the diminishment of plasticity as compared to the reference 316L steel. Besides, the elongation to failure was gradually reduced due to the accumulation of dislocations for longer MA times, especially within fine-grained regions, where the free dislocation motion was restricted and led to quicker localization of plastic deformation.

Finally, it should be pointed out that the tensile properties of specimens milled for 5, 10 and 50 h were nearly identical irrespective of the $Y_2O_3$ particle size, underscoring that MA duration, and resulting microstructure reformation, exerts a more significant influence on mechanical performance rather than oxide particle size. Among the investigated ODS steels, the specimens subjected to the prolonged milling for 50 h, regardless of whether nano- or micro-sized $Y_2O_3$ was used, exhibited the highest YS of ~780-790 MPa. It was ensured by the significant grain refinement (Fig. 3) and the strengthening contribution of $Y_2O_3$ particles (~400 MPa) distributed more homogeneously as compared to shorter milling times. In turn, the ODS steels produced after 5 and 10 h of MA displayed coarser, partially bimodal grain structures with numerous $Y_2O_3$ agglomerates located along grain boundaries leading to the significantly lower YS (360-440 MPa). In these samples, the strengthening contribution of $Y_2O_3$ particles was much weaker (<100 MPa), while the dislocation and grain boundary strengthening mechanisms provided the additional strength as compared to the reference 316L steel (Table 3).

### 4.3. Corrosion properties

The corrosion rate of the investigated materials was strongly influenced by microstructural inhomogeneity, particularly the bimodal grain size distribution, the internal strain introduced during MA (presented in the form of GNDs maps), and the dispersion of $Y_2O_3$ particles within the matrix The lowest corrosion rate, independent of $Y_2O_3$ particle size, was observed in the material subjected to the shortest milling duration (5 h). This behavior can be attributed to the relatively low fraction of ultrafine grains and the lowest dislocation density which together minimized the driving force for localized corrosion. As shown in this study, plastic deformation of ductile austenite during MA introduces a high dislocation density and profoundly modifies both grain morphology and internal stresses, with the extent of these effects increasing with milling time. Therefore, after the longest MA timing the highest corrosion rate was achieved. Additionally, TEM revealed a high density of dislocations within the finest grains, supporting the expectation that materials with the highest fraction of fine grains would exhibit the poorest corrosion resistance. The material produced after 50 h of MA contained the largest proportion of grains below 5 µm, resulting in a high density of grain boundaries, which act as preferential sites for corrosion initiation and propagation. Combined with the pronounced dislocation density observed in those materials, these features explain the rapid penetration of corrosion into the materials' depth, as confirmed by SEM/FIB analyses. These findings indicate that prolonged MA (50 h) does not enhance the corrosion resistance of 316L steel with $Y_2O_3$ addition and, in fact, promoting its degradation. Notably, at this high level of plastic deformation, clear differences emerge between materials containing nano- and micro-sized $Y_2O_3$: the latter exhibits a corrosion rate approximately 1.5 times higher than its nano-sized counterpart. Presumably, this effect was further amplified by the yttria particle size.

Cong et al. [78] showed that the presence of $Y_2O_3$ may promote corrosion reactions because the particle–matrix interface provides a fast diffusion path for alloying elements. Accordingly, larger $Y_2O_3$ interfacial areas increase the susceptibility to corrosion spreading. The areas between yttria agglomerates and matrix of the materials are the easy paths for chlorides penetrations. This would explain faster degradation of the ODS steels with micro-yttria addition sintered after 50 h of MA. Interestingly, our findings contrast with those of Li et al. [79] and Zhang et al. [80] who attributed the improved corrosion resistance of ODS 304 steels to a higher density of grain boundaries and the presence of nano-oxide dispersions decorating these boundaries. In the present work, this configuration appears to facilitate rapid oxygen transport along grain boundaries, effectively acting as a diffusion short-circuit,accelerating corrosion rather than suppressing it.

Corrosion testing revealed that the microstructural changes formed by MA critically determine degradation behavior, and the predominant factor affecting corrosion performance is grain size itself. As proved by Gollapudi et al. [81], the larger volume fraction of grain boundaries compiled with the fine grain sizes are more prone to corrode than the coarse grained material with less grain boundary volume. Therefore, in our case, in chloride containing solutions the more refined microstructure, the lowest corrosion resistance to the solution.

Overall, the study establishes that optimizing MA conditions is

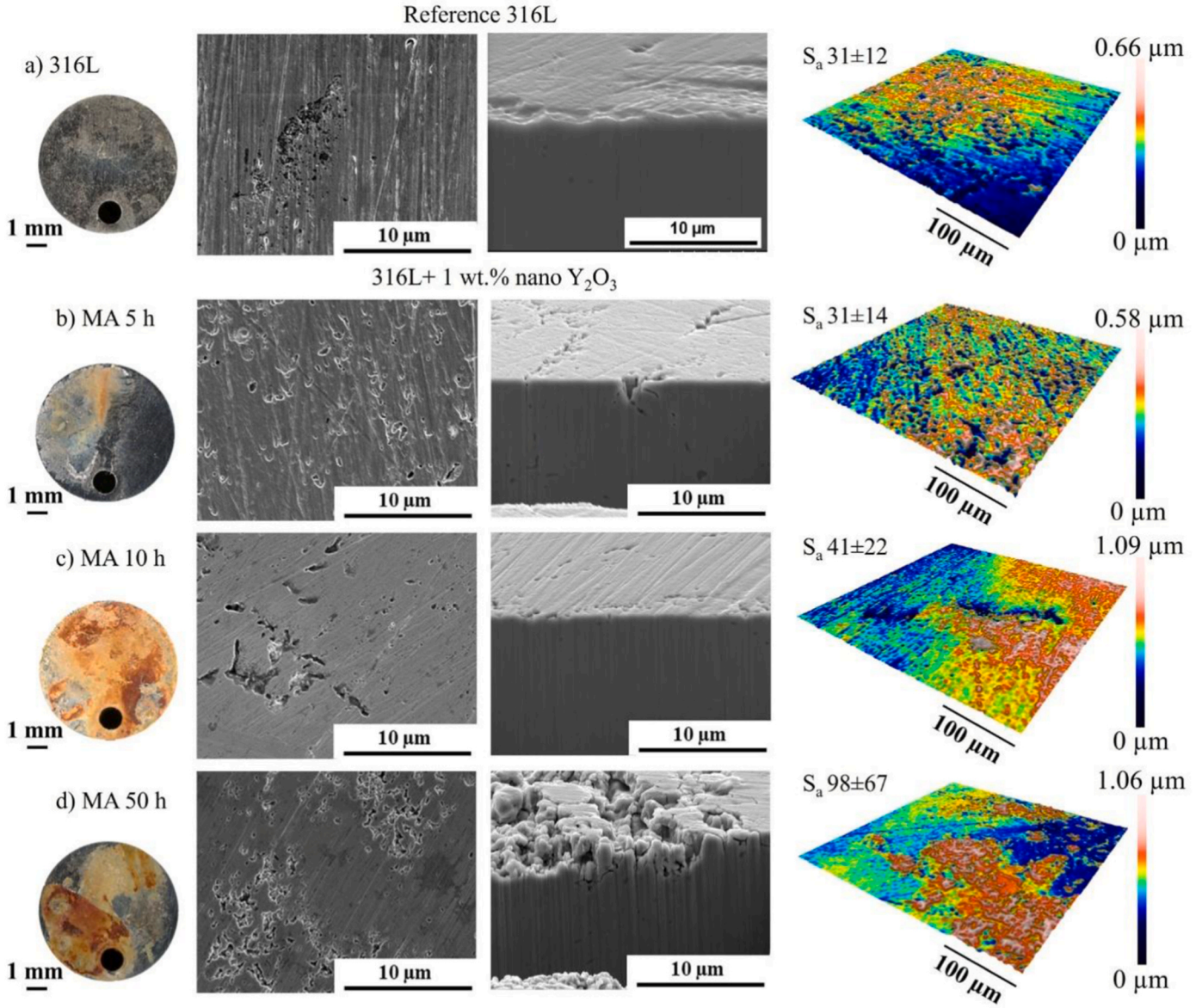


**Fig. 11.** Corrosion damage characterization of the samples after salt spray exposure: a) reference 316L stainless steel, and 316L with the addition of 1 wt% nano-sized $Y_2O_3$ after b) 5 h, c) 10 h and d) 50 h of MA sintered using PPS. In the first column macro images are shown, in the second column SEM images of the surfaces after corrosion products removal with the corresponding cross-sectional observations. In the fourth column 3D maps of the surface development are shown; $S_a$ - arithmetic mean height in nm.

essential for achieving a balanced combination of strength, ductility, and corrosion performance in austenitic ODS steels. The evidence supports the conclusion that processing-induced strain heterogeneity, rather than oxide particle size, governs the evolution of bimodal microstructures and their resultant properties. Consequently, mechanical alloying must be tailored specifically to each alloy composition to control the interplay between microstructural refinement, oxide dispersion, and corrosion stability.

## 5. Conclusions

In this study, new austenitic ODS steels were produced by different MA durations with nano- and micro-sized $Y_2O_3$ particle addition. The investigation led to the following key findings.

- Mechanical alloying (MA) duration was the dominant factor influencing both mechanical and corrosion properties of 316L ODS steels, whereas the size of the $Y_2O_3$ addition had a negligible effect on tensile performance.
- Prolonged MA (50 h) produced the highest-strength ODS steels due to significant grain refinement and more homogeneous distribution of $Y_2O_3$ particles (as compared to shorter milling times), providing additional strengthening at the cost of reduced ductility.
- Corrosion resistance decreased with increasing MA duration. The lowest corrosion rates were measured for specimens milled for 5 h, which exhibited the lowest grain misorientation, smallest fraction of ultrafine grains, and minimal internal strain.
- Materials milled for 50 h showed the poorest corrosion performance, linked to their high density of grain boundaries and dislocations, which acted as preferential paths for corrosion propagation. SEM/FIB confirmed rapid penetration of corrosion into the bulk material.
- At high levels of plastic deformation, $Y_2O_3$ particle size affected corrosion behavior, with steels containing micro-sized $Y_2O_3$

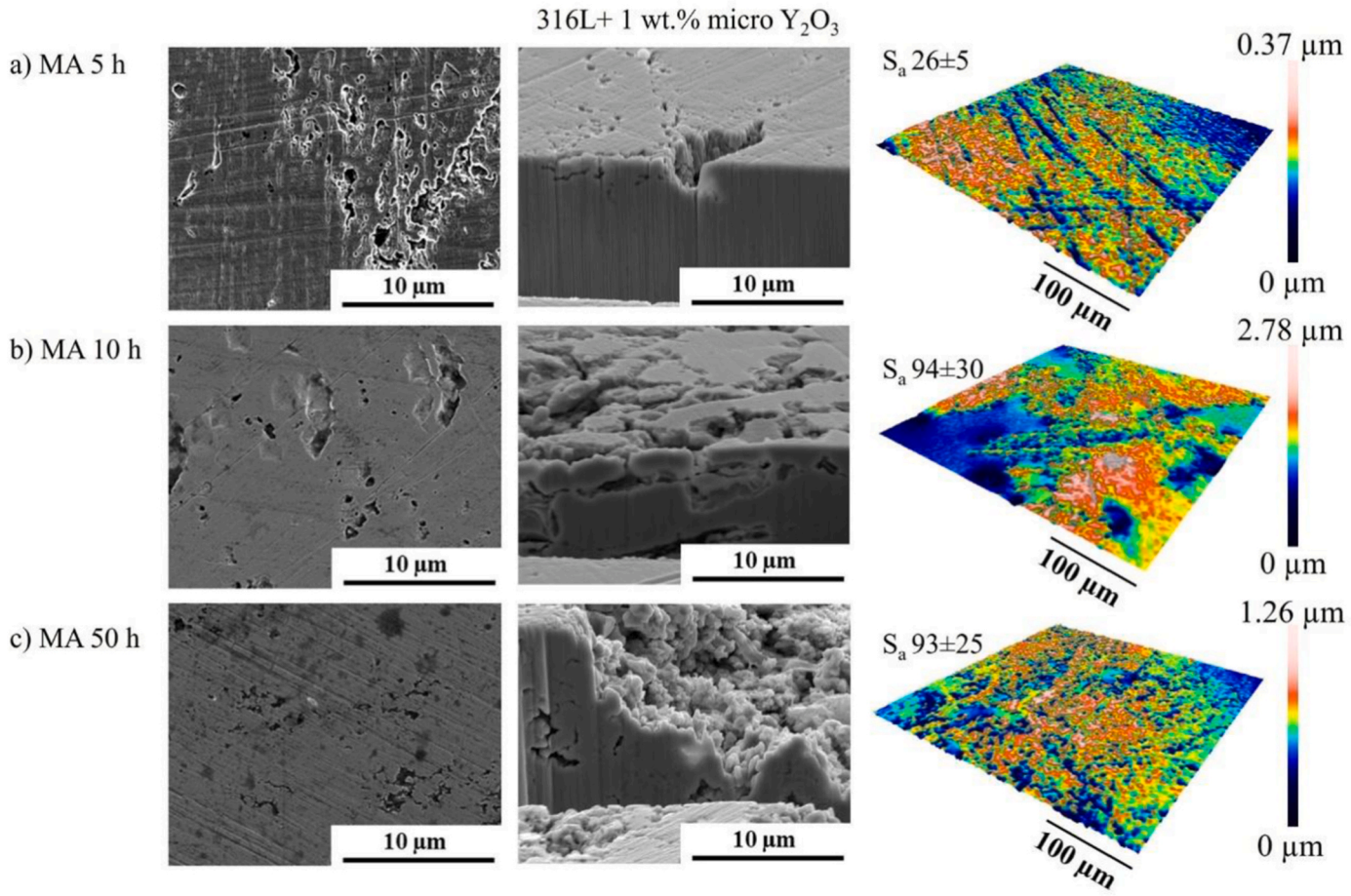


**Fig. 12.** Corrosion damage characterization after salt spray chamber tests of the 316L with the addition of 1 wt% of micro-sized $Y_2O_3$ after b) 5 h, c) 10 h and d) 50 h of MA sintered using PPS. In the first column macro images are shown, in the second column SEM images of the surfaces after corrosion products removal with corresponding cross-sectional observations. In the fourth column 3D maps of the surface development are shown; $S_a$ - arithmetic mean height in nm.

**Table 4**
The estimated contributions of different strengthening mechanisms ($\sigma_0$ – lattice friction, $\sigma_{ss}$ – solid solution strengthening, $\sigma_{gb}$ – grain boundary strengthening, $\sigma_d$ – dislocation strengthening, $\sigma_p$ – particle strengthening).

| Material | MA time | $\sigma_0$ (MPa) | $\sigma_{ss}$ (MPa) | $\sigma_{gb}$ (MPa) | $\sigma_d$ (MPa) | $\sigma_p$ (MPa) |
|---|---|---|---|---|---|---|
| 316L | - | 17 | 139 | 32 | 71 | - |
| 316L + 1 wt% | 5 | 17 | 139 | 106 | 95 | 36 |
| nano-sized | 10 | 17 | 139 | 146 | 109 | 92 |
| $Y_2O_3$ | 50 | 17 | 139 | 222 | 117 | 380 |
| 316L + 1 wt% | 5 | 17 | 139 | 108 | 89 | 46 |
| micro-sized | 10 | 17 | 139 | 126 | 97 | 52 |
| $Y_2O_3$ | 50 | 17 | 139 | 208 | 110 | 415 |

exhibiting corrosion rates approximately 1.5 times higher than their nano-sized counterparts.

- The observed behavior contrasts with several earlier studies, which reported improved corrosion resistance with grain refinement and nano-oxide dispersion. In the present work, the increased grain boundary density and oxide dispersion facilitated oxygen transport and accelerated corrosion.
- These results highlight the need for careful optimization of MA parameters to achieve a balance between mechanical strength and corrosion resistance. Further studies using micro-electrode techniques are recommended to elucidate the local electrochemical activity of $Y_2O_3$ and its role in corrosion processes.

## Declaration of competing interest

The authors declare that they have no known competing financial interests or personal relationships that could have appeared to influence the work reported in this paper.

## Acknowledgments

This research was funded by the National Science Centre, Poland, under the OPUS call in the Weave program (project No.2021/43/I/ST8/01018). This research was also funded by the Czech Science Foundation (project No. 22-04227L) and the Grant agency of the UCT Prague (project No. A2_FCHT_2025_050), and Slovenian Research and Innovation Agency (project No. N2-0276 and core funding No. P2-0132).

## Appendix A. Supplementary data

Supplementary data to this article can be found online at https://doi.org/10.1016/j.jmrt.2026.02.032.

## References

[1] Abram T, Ion S. Generation-IV nuclear power: a review of the state of the science. Energy Policy 2008;36:4323–30. https://doi.org/10.1016/j.enpol.2008.09.059.
[2] Murty KL, Charit I. Structural materials for Gen-IV nuclear reactors: challenges and opportunities. J Nucl Mater 2008;383:189–95. https://doi.org/10.1016/j.jnucmat.2008.08.044.
[3] Zinkle SJ, Was GS. Materials challenges in nuclear energy. Acta Mater 2013;61:735–58. https://doi.org/10.1016/j.actamat.2012.11.004.

[4] Zhou X, Liu C, Yu L, Liu Y, Li H. Phase transformation behavior and microstructural control of High-Cr martensitic/ferritic heat-resistant steels for power and nuclear plants: a review. J Mater Sci Technol 2015;31:235–42. https://doi.org/10.1016/j.jmst.2014.12.001.
[5] De Castro V, Marquis EA, Lozano-Perez S, Pareja R, Jenkins ML. Stability of nanoscale secondary phases in an oxide dispersion strengthened Fe-12Cr alloy. Acta Mater 2011;59:3927–36. https://doi.org/10.1016/j.actamat.2011.03.017.
[6] Hirata A, Fujita T, Wen YR, Schneibel JH, Liu CT, Chen MW. Atomic structure of nanoclusters in oxide-dispersion-strengthened steels. Nat Mater 2011;10:922–6. https://doi.org/10.1038/nmat3150.
[7] Goshchitskii BN, Sagaradze VV, Shalaev VI, Arbuzov VL, Tian Y, Qun W, Jiguang S. Structure, radiation resistance and thermal creep of ODS ferritic steels. J Nucl Mater 2002;307–311:783–7. https://doi.org/10.1016/S0022-3115(02)01047-4.
[8] Shen J, Yang H, Li Y, Kano S, Matsukawa Y, Satoh Y, Abe H. Microstructural stability of an as-fabricated 12Cr-ODS steel under elevated-temperature annealing. J Alloys Compd 2017;695:1946–55. https://doi.org/10.1016/j.jallcom.2016.11.029.
[9] Gao R, Cheng B, Zeng LF, Miao S, Hou J, Zhang T, Wang XP, Fang QF, Liu CS. Microstructure, hardness and defect structure of the He irradiated ODS ferritic steel. J Alloys Compd 2017;691:653–8. https://doi.org/10.1016/j.jallcom.2016.08.312.
[10] Kumar D, Prakash U, Dabhade VV, Laha K, Sakthivel T. High yttria ferritic ODS steels through powder forging. J Nucl Mater 2017;488:75–82. https://doi.org/10.1016/j.jnucmat.2016.12.043.
[11] Wu S, Li J, Li W, Liu S. Characterization of oxide dispersoids and mechanical properties of 14Cr-ODS FeCrAl alloys. J Alloys Compd 2020;814:152282. https://doi.org/10.1016/J.JALLCOM.2019.152282.
[12] Tanno T, Takeuchi M, Ohtsuka S, Kaito T. Corrosion behavior of ODS steels with several chromium contents in hot nitric acid solutions. J Nucl Mater 2017;494:219–26. https://doi.org/10.1016/j.jnucmat.2017.07.008.
[13] Singh R, Prakash U, Kumar D, Laha K. Nano oxide particles in 18Cr oxide dispersion strengthened (ODS) steels with high yttria contents. Mater Char 2022;189:111936. https://doi.org/10.1016/j.matchar.2022.111936.
[14] Ordás N, Gil E, Cintins A, de Castro V, Leguey T, Iturriza I, Purans J, Anspoks A, Kuzmin A, Kalinko A. The role of yttrium and titanium during the development of ODS ferritic steels obtained through the STARS route: TEM and XAS study. J Nucl Mater 2018;504:8–22. https://doi.org/10.1016/j.jnucmat.2018.03.020.
[15] Zhao R, Jia H, Cao S, Tong Z, Zhou Z. Effect of the addition of Y and Y2O3 on microstructure and mechanical properties of 15Cr-15Ni ODS steel. Nucl Mater Energy 2022;31:101196. https://doi.org/10.1016/j.nme.2022.101196.
[16] Takaya S, Furukawa T, Aoto K, Müller G, Weisenburger A, Heinzel A, Inoue M, Okuda T, Abe F, Ohnuki S, Fujisawa T, Kimura A. Corrosion behavior of Al-alloying high Cr-ODS steels in lead-bismuth eutectic. J Nucl Mater 2009;386–388:507–10. https://doi.org/10.1016/j.jnucmat.2008.12.155.
[17] Lee JH, Kasada R, Kimura A, Okuda T, Inoue M, Ukai S, Ohnuki S, Fujisawa T, Abe F. Influence of alloy composition and temperature on corrosion behavior of ODS ferritic steels. J Nucl Mater 2011;417:1225–8. https://doi.org/10.1016/j.jnucmat.2010.12.279.
[18] Ningshen S, Sakairi M, Suzuki K, Ukai S. The corrosion resistance and passive film compositions of 12% Cr and 15% Cr oxide dispersion strengthened steels in nitric acid media. Corros Sci 2014;78:322–34. https://doi.org/10.1016/j.corsci.2013.10.015.
[19] Kimura A, Kasada R, Iwata N, Kishimoto H, Zhang CH, Isselin J, Dou P, Lee JH, Muthukumar N, Okuda T, Inoue M, Ukai S, Ohnuki S, Fujisawa T, Abe TF. Development of Al added high-Cr ODS steels for fuel cladding of next generation nuclear systems. J Nucl Mater 2011;417:176–9. https://doi.org/10.1016/j.jnucmat.2010.12.300.
[20] Xu H, Lu Z, Wang D, Liu C. Microstructural evolution in a new Fe based ODS alloy processed by mechanical alloying. Nucl Mater Energy 2016;7:1–4. https://doi.org/10.1016/j.nme.2016.04.006.
[21] Sun QX, Fang QF, Zhou Y, Xia YP, Zhang T, Wang XP, Liu CS. Development of oxide dispersion strengthened ferritic steel prepared by chemical reduction and mechanical milling. J Nucl Mater 2013;439:103–7. https://doi.org/10.1016/j.jnucmat.2013.03.087.
[22] Li Y, Shen J, Li F, Yang H, Kano S, Matsukawa Y, Satoh Y, Fu H, Abe H, Muroga T. Effects of fabrication processing on the microstructure and mechanical properties of oxide dispersion strengthening steels. Mater Sci Eng A 2016;654:203–12. https://doi.org/10.1016/j.msea.2015.12.032.
[23] Cha SI, Hong SH, Kim BK. Spark plasma sintering behavior of nanocrystalline WC–10Co cemented carbide powders. Mater Sci Eng A 2003;351:31–8. https://doi.org/10.1016/S0921-5093(02)00605-6.
[24] Feng P, Xiong W, Yu L, Zheng Y, Xia Y. Phase evolution and microstructure characteristics of ultrafine Ti(C,N)-based cermet by spark plasma sintering. Int J Refract Met Hard Mater 2004;22:133–8. https://doi.org/10.1016/j.ijrmhm.2004.03.002.
[25] Bordia R, Olevsky E. Advances in sintering science and technology. J Am Ceram Soc 2009;92:1383. https://doi.org/10.1111/j.1551-2916.2009.03241.x. 1383.
[26] Kruszewski MJ, Zybała R, Ciupiński, Chmielewski M, Adamczyk-Cieślak B, Michalski A, Rajska M, Kurzydłowski KJ. Microstructure and thermoelectric properties of bulk cobalt antimonide (CoSb3) skutterudites obtained by pulse plasma sintering. J Electron Mater 2016;45:1369–76. https://doi.org/10.1007/s11664-015-4037-5.
[27] Kimura A. Current status of reduced-activation ferritic/martensitic steels R&D for fusion energy. Mater Trans 2005;46:394–404. https://doi.org/10.2320/matertrans.46.394.
[28] Odette GR. Recent progress in developing and qualifying nanostructured ferritic alloys for advanced fission and fusion applications. Jom 2014;66:2427–41. https://doi.org/10.1007/s11837-014-1207-5.
[29] Oksiuta Z, Olier P, de Carlan Y, Baluc N. Development and characterisation of a new ODS ferritic steel for fusion reactor application. J Nucl Mater 2009;393:114–9. https://doi.org/10.1016/j.jnucmat.2009.05.013.
[30] Sokolov MA, Hoelzer DT, Stoller RE, McClintock DA. Fracture toughness and tensile properties of nano-structured ferritic steel 12YWT. J Nucl Mater 2007;367–370 A:213–6. https://doi.org/10.1016/j.jnucmat.2007.03.143.
[31] Luptáková N, Svoboda J, Bártková D, Weiser A, Dlouhý A. The irradiation effects in ferritic, ferritic–martensitic and austenitic oxide dispersion strengthened alloys. A Review, Materials (Basel) 2024;17. https://doi.org/10.3390/ma17143409.
[32] Balázsi C, Gillemot F, Horváth M, Wéber F, Balázsi K, Sahin FC, Onüralp Y, Horváth Á. Preparation and structural investigation of nanostructured oxide dispersed strengthened steels. J Mater Sci 2011;46:4598–605. https://doi.org/10.1007/s10853-011-5359-1.
[33] Gräning T, Rieth M, Hoffmann J, Möslang A. Production, microstructure and mechanical properties of two different austenitic ODS steels. J Nucl Mater 2017;487:348–61. https://doi.org/10.1016/j.jnucmat.2017.02.034.
[34] Vaishnavi VK, Dasgupta A, Ghosh C, Sinha SK. Analysis of structural transformation in nanocrystalline Y2O3 during high energy ball milling. J Alloys Compd 2022;900:163550. https://doi.org/10.1016/J.JALLCOM.2021.163550.
[35] Laptev AM, Bram M, Garbiec D, Räthel J, van der Laan A, Beynet Y, Huber J, Küster M, Cologna M, Guillon O. Tooling in spark plasma sintering technology: design, optimization, and application. Adv Eng Mater 2024;26. https://doi.org/10.1002/adem.202301391.
[36] Molak RM, Paradowski K, Brynk T, Ciupinski L, Pakiela Z, Kurzydlowski KJ. Measurement of mechanical properties in a 316L stainless steel welded joint. Int J Pres Ves Pip 2009;86:43–7. https://doi.org/10.1016/j.ijpvp.2008.11.002.
[37] Majchrowicz K, Romelczyk-Baishya B, Wieczorek-Czarnocka M, Dobkowska A, Raga K, Filip R, Pakieła Z. Determination of the fracture toughness of carburized Pyrowear 53 steel for planetary gears by the small punch test method. Arch Civ Mech Eng 2024;24. https://doi.org/10.1007/s43452-024-00992-9.
[38] Sitek R, Puchlerska S, Nejman I, Majchrowicz K, Pakieła Z, Żaba K, Mizera J. The impact of plastic deformation on the microstructure and tensile strength of haynes 282 nickel superalloy produced by DMLS and casting. Materials 2022;15. https://doi.org/10.3390/ma15217545.
[39] I. 6892-1:2019 [IDT] EN ISO 6892-1:2019 [IDT], metals – tensile test – part 1: room temperature test method, KT 123, Res Prop Met (n.d) 92.
[40] ISO 6506-1. Metallic materials — Brinell hardness test part 1: test method. third ed. ISO; 2014. https://www.iso.org/standard/59671.html.
[41] International Organization for Standardization (ISO). PN-EN ISO 9227:2012; corrosion testing in artificial atmospheres—salt spray. In: Polish committee for standardization: warsaw, Poland, 2012, Warsaw, Poland; 2012.
[42] Anon. Standard practice for preparing, cleaning, and evaluating corrosion test specimens, i. ASTM Spec. Tech. Publ.; 1985. p. 505–10. https://doi.org/10.1520/G0001-03R17E01.2.
[43] Lin Deng WZ, Jin-ru Luo, Tu Jian, Hu Rong, Guo Ning, Chang-hao Wang YZ, He Pei. Achieving excellent mechanical properties of ODS steel by Y2O3 addition. Mater Sci Eng A 2023;872. https://doi.org/10.1016/j.msea.2023.145008.
[44] Mayer M, Svoboda J, Mendez-Martin F, Fellner S, Gammer C, Razumovskiy V, Resch L, Sprengel W, Stark A, Zeisl S, Ressel G. From microscopic to atomistic scale: temperature effect on yttria distribution in mechanically alloyed FeCrMnNiCo powder particles. J Alloys Compd 2023;968:171850. https://doi.org/10.1016/j.jallcom.2023.171850.
[45] Wang M, Zhou Z, Sun H, Hu H, Li S. Microstructural observation and tensile properties of ODS-304 austenitic steel. Mater Sci Eng A 2013;559:287–92. https://doi.org/10.1016/j.msea.2012.08.099.
[46] Kumar SS, Sandeep ES, Chandrasekhar SB, Karak SK. Development of nano-oxide dispersed 304L steels by mechanical milling and conventional sintering. Mater Res 2016;19:175–82. https://doi.org/10.1590/1980-5373-MR-2015-0593.
[47] Ninawe PS, Ganesh S, Sai Karthik P, Chandrasekhar SB, Vijay R. Microstructure and mechanical properties of spark plasma sintered austenitic ODS steel. Adv Powder Technol 2022;33:103584. https://doi.org/10.1016/j.apt.2022.103584.
[48] Suresh K, Nagini M, Vijay R, Ramakrishna M, Gundakaram RC, Reddy AV, Sundararajan G. Microstructural studies of oxide dispersion strengthened austenitic steels. Mater Des 2016;110:519–25. https://doi.org/10.1016/j.matdes.2016.08.020.
[49] Okuda T, Fujiwara M. Dispersion behaviour of oxide particles in mechanically alloyed ODS steel. J Mater Sci Lett 1995;14:1600–3. https://doi.org/10.1007/BF00455428.
[50] Singh Ratnakar, Prakash Ujjwal. P/M 18Cr ODS steels produced by mechanical alloying and hot powder forging. Powder Technol 2023;429:118967. https://doi.org/10.1016/j.powtec.2023.118967.
[51] Jasinski JJ, Stasiak T, Chmurzynski W, Kurpaska L, Chmielewski M, Frelek-Kozak M, Wilczopolska M, Mulewska K, Zielinski M, Kowal M, Diduszko R, Chrominski W, Jagielski J. Microstructure and phase investigation of FeCrAl-Y2O3 ODS steels with different Ti and V contents. J Nucl Mater 2023;586. https://doi.org/10.1016/j.jnucmat.2023.154700.
[52] Chauhan A, Litvinov D, Aktaa J. Deformation and damage mechanisms of a bimodal 12Cr-ODS steel under high-temperature cyclic loading. Int J Fatig 2016;93:1–17. https://doi.org/10.1016/j.ijfatigue.2016.08.003.
[53] Lu C, Lu Z, Wang X, Xie R, Li Z, Higgins M, Liu C, Gao F, Wang L. Enhanced radiation-tolerant oxide dispersion strengthened steel and its microstructure evolution under helium-implantation and heavy-ion irradiation. Sci Rep 2017;7:1–7. https://doi.org/10.1038/srep40343.

[54] Boulnat X, Perez M, Fabregue D, Douillard T, Mathon MH, De Carlan Y. Microstructure evolution in nano-reinforced ferritic steel processed by mechanical alloying and spark plasma sintering. Metall Mater Trans A Phys Metall Mater Sci 2014;45:1485–97. https://doi.org/10.1007/s11661-013-2107-y.
[55] García-Rodríguez N, Campos M, Torralba JM, Berger MH, Bienvenu Y. Capability of mechanical alloying and SPS technique to develop nanostructured high Cr, Al alloyed ODS steels. Mater Sci Technol 2014;30:1676–84. https://doi.org/10.1179/1743284714Y.0000000595.
[56] Alaneme KK, Okotete EA. Recrystallization mechanisms and microstructure development in emerging metallic materials: a review. J Sci Adv Mater Devices 2019;4:19–33. https://doi.org/10.1016/j.jsamd.2018.12.007.
[57] Hansen N. Hall – petch relation and boundary strengthening, vol. 51; 2004. p. 801–6. https://doi.org/10.1016/j.scriptamat.2004.06.002.
[58] Chauhan A, Bergner F, Etienne A, Aktaa J, De Carlan Y, Heintze C. Microstructure characterization and strengthening mechanisms of oxide dispersion strengthened (ODS) Fe-9 % Cr and Fe-14 % Cr extruded bars 2017;495:6–19. https://doi.org/10.1016/j.jnucmat.2017.07.060.
[59] Kamikawa N, Sato K, Miyamoto G, Murayama M, Sekido N. ScienceDirect stress – strain behavior of ferrite and bainite with nano-precipitation in low carbon steels. Acta Mater 2015;83:383–96. https://doi.org/10.1016/j.actamat.2014.10.010.
[60] Queyreau S, Monnet G, Devincre B. Orowan strengthening and forest hardening superposition examined by dislocation dynamics simulations. Acta Mater 2010;58:5586–95. https://doi.org/10.1016/j.actamat.2010.06.028.
[61] Science M. Study of the peierls-nabarro. 1997.
[62] Friction I. Moduli and internal friction of low carbon and stainless steels as a function ot. Temperature (Austin) 1993;33:508–12.
[63] Schmauder S, Kohler C. Atomistic simulations of solid solution strengthening of a -iron 2011;50:1238–43. https://doi.org/10.1016/j.commatsci.2010.04.041.
[64] Mohd S, Chen Y, Yang S, Gao N. Materials characterization microstructural evolution and strengthening of selective laser melted 316L stainless steel processed by high-pressure torsion. Mater Char 2020;159:110012. https://doi.org/10.1016/j.matchar.2019.110012.
[65] Eliasson J, Sandstrom R. Proof strength values for austenitic stainless steels at elevated temperatures, vol. 71; 2000. p. 249–54.
[66] Chen S, Ma G, Wu G, Godfrey A, Huang T. Materials science & engineering A strengthening mechanisms in selective laser melted 316L stainless steel. Mater Sci Eng A 2022;832:142434. https://doi.org/10.1016/j.msea.2021.142434.
[67] Hall EO. The deformation and ageing of mild steel: III discussion of results. Proc Phys Soc B 1951;64:747–53. https://doi.org/10.1088/0370-1301/64/9/303.
[68] ThisWeek ' s Citation Classic _____; 1982. p. 1982.
[69] Kashyap BP, Tangri K. ON the HALL-petch relationship a N D S U B S T R U C T U R a L evolution in type 316L stainless steel. 1995. p. 43.
[70] Reproduced with permission of the copyright owner. Further reproduction prohibited without permission., (n.d).
[71] V Astafurov S, Maier GG, V Melnikov E, Moskvina VA, Panchenko MY, Astafurova EG. Materials Science & Engineering A The strain-rate dependence of the Hall-Petch e ff ect in two austenitic stainless steels with di ff erent stacking fault energies. Mater Sci Eng A 2019;756:365–72. https://doi.org/10.1016/j.msea.2019.04.076.
[72] Dyakonov GS, Zemtsova E, Mironov S, Semenova IP, Valiev RZ, Semiatin SL. Materials science & engineering A an EBSD investigation of ultra fi ne-grain titanium for biomedical applications. Mater Sci Eng A 2015;648:305–10. https://doi.org/10.1016/j.msea.2015.09.080.
[73] Majchrowicz K, Sotniczuk A, Garbacz H. J Alloys Compd 2023:948. https://doi.org/10.1016/j.jallcom.2023.169791.
[74] Character P, Jul N. The mechanism of plastic deformation of crystals . Part I . Theoretical author (s): g . I . Taylor source. In: Proceedings of the royal society of London . Series A , containing papers of a published by : Royal society stable, vol. 145; 1934. p. 362–87. URL : https://www.jstor.org/stable/2935509REFERENCESLinkedreferencesareavailableonJSTORforthisarticle:reference#references_tab_contentsYoumayneedtologintoJSTORtoaccessthelinkedreferences.
[75] Stoller RE, Zinkle SJ. On the relationship between uniaxial yield strength and resolved shear stress in polycrystalline. Materials 2008;287:349–52.
[76] Hansen N, Huang X. Microstructure and flow stress of polycrystals and single crystals, vol. 46; 1998. p. 1827–36.
[77] García-Junceda A, Campos M, García-Rodríguez N, Torralba JM. On the role of alloy composition and sintering parameters in the bimodal grain size distribution and mechanical properties of ODS ferritic steels. Metall Mater Trans A Phys Metall Mater Sci 2016;47:5325–33. https://doi.org/10.1007/s11661-016-3538-z.
[78] Cong S, Gao Y, Liu Z, Peng W, Zhang Y, Ma L, Zhou Z, Zhang L, Guo X. Role of Al addition and Y2O3 on the intergranular corrosion behavior of AFA-ODS steel in the supercritical water. Mater Des 2022;224. https://doi.org/10.1016/j.matdes.2022.111386.
[79] Li SF, Zhou ZJ, Zhang LF, Zhang LW, Hu HL, Wang M, Zhang GM. Corrosion behavior of a 304-oxide dispersion strengthened austenitic stainless steel in supercritical water. Mater Corros 2016;67:264–70. https://doi.org/10.1002/maco.201508359.
[80] Zhang W, Liu F, Liu L, Li Q, Liu L, Liu F, Huang C. Effect of grain size and distribution on the corrosion behavior of Y2O3 dispersion-strengthened 304 stainless steel. Mater Today Commun 2022;31:103723. https://doi.org/10.1016/j.mtcomm.2022.103723.
[81] Gollapudi S. Grain size distribution effects on the corrosion behaviour of materials. Corros Sci 2012;62:90–4. https://doi.org/10.1016/j.corsci.2012.04.040.